Cape Verde Frontal Zone in summer 2017: lateral transports of mass, dissolved oxygen and inorganic nutrients

Nadia Burgoa[1], Francisco Machín[1], Ángel Rodríguez-Santana[1], Ángeles Marrero-Díaz[1], Xosé Antón Álvarez-Salgado[2], Bieito Fernández-Castro[3], María Dolores Gelado-Caballero[4], and Javier Arístegui[5]

[1]Departamento de Física, Universidad de Las Palmas de Gran Canaria, Spain
[2]CSIC Instituto de Investigacións Mariñas, Vigo, Spain
[3]Ocean and Earth Science, University of Southampton, United Kingdom
[4]Departamento de Química, Universidad de Las Palmas de Gran Canaria, Spain
[5]Instituto de Oceanografía y Cambio Global, Universidad de Las Palmas de Gran Canaria, Spain

Correspondence: Nadia Burgoa (nadia.burgoa@ulpgc.es)

Abstract.

The circulation patterns in the confluence of the North Atlantic Subtropical and Tropical gyres delimited by the Cape Verde Front (CVF) were examined during a field cruise in summer 2017. We collected hydrographic data, dissolved oxygen (O_2) and inorganic nutrients along the perimeter of a closed box embracing the Cape Verde Frontal Zone (CVFZ). The detailed

5   spatial (horizontal and vertical) distribution of water masses, O_2 and inorganic nutrients in the CVF was analyzed, allowing to estimate independently the transports of these properties in the subtropical and tropical domains down to 2000 m. Overall, at surface and central levels a net westward transport of 3.76 Sv was observed, while at intermediate levels a net 3 Sv transport northward was obtained. We observed O_2 and inorganic nutrients imbalances in the domain consistent with O_2 consumption and inorganic nutrients production by organic matter remineralization, resulting in a net transport of inorganic nutrients to the

10   ocean interior by the circulation patterns.

1 INTRODUCTION

The Cape Verde Basin (CVB) is located in the eastern boundary of the North Atlantic Ocean at the meeting point of the subtropical and tropical domains. This area is influenced by the North Atlantic subtropical gyre, NASG (Stramma and Siedler, 1988), the North Atlantic tropical gyre, NATG (Siedler et al., 1992), and the upwelling region off NW Africa (Ekman, 1923;

15   Tomczak, 1979; Hughes and Barton, 1974; Hempel, 1982). In the central waters level (from 100 to 650-700 m depth) within this domain, the Cape Verde Frontal Zone (CVFZ) extents from Cape Blanc to Cape Verde Islands as a northeast-southwest boundary between subtropical and tropical waters (Zenk et al., 1991). In addition, the Coastal Upwelling Front (CUF) along the Mauritanian coast, until Cape Blanc/Cape Verde in summer/winter separates stratified oceanic waters and more homogeneous slope waters in the CVB (Benazzouz et al., 2014a, b; Pelegrí and Benazzouz, 2015a). These two frontal systems also act as a

20   dynamic source of mesoscalar and submesoscalar variability related to interleaving mixing processes and filaments associated

with the CUF (Pérez-Rodríguez et al., 2001; Martínez-Marrero et al., 2008; Capet et al., 2008; Thomas, 2008; Meunier et al., 2012; Hosegood et al., 2017).

The northern side of the CVFZ is mainly occupied by an ensemble of subtropical waters, generically denominated as Eastern North Atlantic Central Water (ENACW), which flows southward transported by the Canary Current (CC). Once the CC approaches the CVFZ, it turns offshore as the North Equatorial Current (NEC) (Stramma, 1984), giving rise to a shadow zone of poorly ventilated waters (Luyten et al., 1983). Additionally, long-lived eddies generated downstream of the Canary Islands (Sangrà et al., 2009; Barceló-Llull et al., 2017) significantly contribute to the westward circulation within the CVB (Sangrà et al., 2009). Between the Canary Islands and Cape Blanc, the steady trade winds force a permanent upwelling (Benazzouz et al., 2014a), which in turn triggers an intense southward coastal jet, the Canary Upwelling Current (CUC) (Pelegrí et al., 2005, 2006). Below the CUC and over the continental slope, the Poleward Undercurrent (PUC) flows northward with remarkable intensity (Barton, 1989; Machín and Pelegrí, 2009; Machín et al., 2010).

The South Atlantic Central Water (SACW) is the main water mass in the southern side of the CVFZ. SACW is formed at the subtropical South Atlantic and it largely modifies its thermohaline features along its complex path northward to the CVB (Peña-Izquierdo et al., 2015). The northern branch of the North Equatorial Counter-current becomes the Cape Verde Current (CVC) at the African Slope carrying SACW (Peña-Izquierdo et al., 2015; Pelegrí et al., 2017). The CVC flows anticlockwise around the Guinea Dome (GD) to the southern part of the CVFZ (Peña-Izquierdo et al., 2015; Pelegrí et al., 2017). A seasonal pattern has been documented, whereby the GD intensifies in summer as a result of the northward penetration of the Inter-Tropical Converge Zone (ITCZ) (Siedler et al., 1992; Castellanos et al., 2015). In addition, the northward flow along the African coast intensifies also in summer due to the relaxation of the trade winds south of Cape Blanc, so the Mauritanian Current (MC) and the PUC increase their northward progression to just south of Cape Blanc (Siedler et al., 1992; Lázaro et al., 2005).

The encountering of southward-flowing CC/CUC with northward-flowing PUC/MC leads to a confluence at the CVFZ, which fosters the offshore export of mass and seawater properties, with its maximum strength in summer (Pastor et al., 2008). Subtropical and tropical waters exported along the CVFZ exhibit distinct physical-chemical properties. ENACW is a relatively young, salty and warm water mass with low nutrient and high oxygen concentrations. SACW is an older water mass fresher and colder than ENACW, largely modified while traveling through tropical regions; hence, SACW at the CVFZ is a nutrient-rich and oxygen-poor water mass (Tomczak, 1981; Zenk et al., 1991; Pastor et al., 2008; Martínez-Marrero et al., 2008; Pastor et al., 2012; Peña-Izquierdo et al., 2015). The CVF drives nutrient-rich SACW into the southeastern edge of the nutrient-poor NASG, a process that boosts a high primary production area offshore as revealed by the giant filament at Cape Blanc (Gabric et al., 1993; Pastor et al., 2013).

Intermediate levels (∼700-1500 m depth) are essentially occupied by modified Antarctic Intermediate Water (AAIW), a relatively fresh and cold water mass with high inorganic nutrient and low O_2 concentrations. At this latitude, AAIW flows northward at 700-1100 m depth along the eastern margin of both the NASG and NATG (Machín et al., 2006; Machín and Pelegrí, 2009; Machín et al., 2010).

The distribution of O_2 and inorganic nutrients below the euphotic layer is determined by biogeochemical and physical processes (Pelegrí and Benazzouz, 2015b). The main biogeochemical processes are related with the availability of organic matter, O_2 and inorganic nutrients at the source regions and also with remineralization processes; on the other hand, the main physical processes are associated with both the vertical link between surface and subsurface waters and also with the lateral transports at subsurface waters (Peña-Izquierdo et al., 2015; Pelegrí and Benazzouz, 2015b). As a consequence, the O_2 and inorganic nutrients concentrations may vary depending on the interplay between the local rate of organic matter remineralization and the rate of water supply (Pelegrí and Benazzouz, 2015b). In other words, the different dynamics between subtropical and tropical regions separated by the CVFZ, and between oceanic and upwelling regions separated by the CUF, establish distinct biogeochemical domains with substantial differences in their O_2 and inorganic nutrient patterns at the CVB. In the last two decades, several authors focused on the O_2 and inorganic nutrient distribution considering both the physical properties of water masses and the dynamical processes involved at varying scales (Pelegrí et al., 2006; Machín et al., 2006; Pastor et al., 2008; Álvarez and Álvarez-Salgado, 2009; Peña-Izquierdo et al., 2012; Pastor et al., 2013; Peña-Izquierdo et al., 2015; Hosegood et al., 2017; Burgoa et al., 2020).

Here we address the circulation patterns and the physical processes behind the distribution of O_2 and inorganic nutrients at the dynamically complex CVFZ. To achieve this goal we used field observations obtained during the FLUXES-I cruise, and applied an inverse model to estimate the mass transports. Additional methods are applied to asses the water masses distribution both horizontally and with depth, to extend the classical definition of the CVF, in order to consistently separate the tropical and subtropical sides.

2 DATA AND METHODOLOGY

2.1 The oceanographic cruise

The FLUXES (Carbon Fluxes in a Coastal Upwelling System – Cape Blanc, NW Africa) project included two cruises during 2017 labeled as FLUXES-I and FLUXES-II. The cruise FLUXES-I provided the dataset to conduct the analyzes presented in this manuscript. It was carried out from July 14th to August 8th 2017 aboard the R/V Sarmiento de Gamboa. A grid of 35 stations was selected to form a closed box (pink dots, Fig. A1). At each station we sampled the water column with a SBE 38 rosette sampler equipped with 24 Niskin bottles of 12 L. Temperature, conductivity and oxygen were measured with a vertical resolution of 1 dbar down to at least 2000 m by means of a CTD SBE 911+. The average distance between neighboring CTD stations was about 84 km. Shallow stations 1 and 29 were discarded from the analysis. The sample grid was split into four transects: the northern transect (N) spanned zonally from station 2 to 12 at 23°N; the western transect (W) was located at 26°W from station 12 to 19; the southern transect (S) at 17.5°N extended from station 19 to 28, while the eastern transect (E) closed the box approximately at 18.6°W from station 28 to 3.

A second observational dataset consisted of 39 expendable bathythermograph probes (XBT, T5 by Sippican) deployed between most CTD stations (blue dots, Fig. A1). WinMK21 acquisition software was setup to sample down to 2000 m, a

sampling aided by a reduced boat speed during XBT deployment (5 kn). Some XBTs (12, 19, 30, 31, 38, 39 and 40) were discarded due to malfunction during recording.

Practical salinity (S_P, UNESCO (1985)) was calibrated after analyzing 51 water samples with a Portasal model 8410A salinometer, attaining an accuracy and precision within the values recommended by WOCE. An oxygen sensor SBE43 was interfaced with the CTD system during the cruise, whose observations were later calibrated with 417 *in situ* samples providing a final precision of $\pm 0.53\ \mu\mathrm{mol\ kg^{-1}}$.

Regarding dissolved inorganic nutrients (nitrates, NO_3, phosphates, PO_4, and silicates, SiO_4H_4), 419 water samples were collected by Niskin bottles and transferred to 25 mL polyethylene bottles. These samples were frozen at -20°C before their analysis using a segmented flow Alliance Futura analyzer following the colorimetric methods proposed by Grasshoff et al. (1999).

2.2 Supplementary datasets

The Ekman transport through the boundaries of the domain was estimated with daily global wind field observations produced with the scatterometer ASCAT installed on the EUMETSAT METOP satellite. This dataset presents a spatial resolution of $0.25°$ (Bentamy and Fillon, 2012) and are made available by CERSAT (ftp://ftp.ifremer.fr/ifremer/cersat/products/gridded/MWF/L3/ASCAT/Daily/). Freshwater flux was calculated from the average rates of evaporation and precipitation extracted from the Weather Research and Forecasting model (WRF, Powers et al. (2017)) provided with a spatial resolution of $0.125°$ and a temporal resolution of 12 h.

The climatological mean depths of the neutral density field during the summer season were evaluated from the climatological temperature and salinity fields extracted from the World Ocean Atlas 2018 (WOA18, Locarnini et al. (2018); Zweng et al. (2018)). WOA18 was also used to produce a climatological neutral density field during the summer season to estimate a climatological geostrophic velocity field. Summer WOA18 nodes were used to extend transects N and S up to the African coast (green dots, Fig. A1). Finally, two WOA stations were selected to apply the methodology developed in this manuscript to unveil the vertical location of the CVF (see section 2.4, Fig. A2).

SEALEVEL_GLO_PHY_L4_REP_OBSERVATIONS_008_047 product issued by Copernicus Marine Environment Monitoring Service (CMEMS, http://marine.copernicus.eu) provided Level-4 Sea Surface Height (SSH) and derived variables as surface geostrophic currents, measured by multi-satellite altimetry observations over the global ocean with a spatial resolution of $0.25°$. These data captured the mesoscale structures and were helpful to validate the near-surface geostrophic field produced by the inversion.

GLORYS 12V1 (GLOBAL_REANALYSIS_PHY_001_030) outputs from 25 years also issued by CMEMS were used to estimate a summer climatology for the velocity field, temperature and salinity, with a horizontal resolution of $1/12°$ at 50 standard depths. Specifically, the climatological salinity was used to present the CVF spatial distribution within the domain (see section 3.2, Fig. A10a).

Data treatments (*in situ*, operational and modelling), interpolations with Data-Interpolating Variational Analysis (DIVA, (Troupin et al., 2012)), graphical representations, and the inverse model were coded in MATLAB (MATLAB, 2019). Finally, the Smith–Sandwell bathymetry V19.1 (Smith and Sandwell, 1997) was used in all maps and full-depth vertical sections.

2.3 Merged hydrographic dataset

A high resolution *in situ* temperature field (T) was produced after merging the CTD and XBT profiles. The remaining variables were interpolated to this same new high resolution grid to perform additional data treatments.

S_P, O_2, NO_3, PO_4 and SiO_4H_4 were optimally interpolated with DIVA at each transect independently. Before carrying out these interpolations, DIVA was applied to the T suppressing one xbt profile from each transect to validate the method. In fact, the interpolated values had a relative error $< 3.5\%$ in 75% of cases. This allows to set the signal to noise ratio (λ) and the horizontal and vertical correlation lengths (L_x and L_y). Hence, the interpolations of the remaining hydrological and biogeochemical variables were carried out with the following parameters: $\lambda = 4$, $L_x = 110 - 135$ km and $L_y = 50$ m. Despite the fact that each variable behaves differently depending on its physical, chemical or biological nature, the correlation scales were considered the same due to the limitation of the sampling resolution. DIVA provided error maps for the gridded fields of each variable which allowed us to check their accuracy and spatial distribution. 75% of the interpolated values of S_P and O_2 had a relative error $\leq 3.5\%$. Due to the lower sampling resolution of NO_3, PO_4 and SiO_4H_4, their interpolated values had higher errors. Between 70-75% of the interpolated values had a relative error $\leq 5.7\%$.

Once the interpolations were performed, Absolute Salinity (S_A, McDougall et al. (2012)), Potential and Conservative Temperatures (θ and Θ, McDougall and Barker (2011)) were calculated (IOC et al., 2010). In addition, neutral density (γ_n, Jackett and McDougall (1997)) was used as the density variable.

2.4 Tracking the Cape Verde Front

One of the main goals of our study was to estimate the lateral fluxes in the tropical and subtropical sides of the Cape Verde Front. For this, we have first to uncover the location of the front both in depth and along its spatial distribution within the domain. The classical definition places the CVF where the isohaline 36 meets the 150 m isobath. Here we have developed a method to extend this definition vertically as follows: two climatological profiles from WOA18 representative of the ENACW and SACW consistent with the definitions given by Tomczak (1981) were selected (Fig. A2a). Those selected climatological profiles provide an average relationship between S_P, θ, and depth, which reveals that the traditional definition of the front is based on a salinity value (36) that corresponds indeed to equal contributions (50%) of ENACW and SACW at 150 m depth. Following the same reasoning of equal contribution, we calculated the climatological salinity that would define the front location at standard depths from 100 to 650 m (Fig. A2b).

Finally, three linear, quadratic and cubic relationships between salinity and depth were used to infer the salinity that would define the front location at any given depth. The quadratic relationship was finally chosen due to its tight fit to observations ($R^2 = 0.998$) keeping the polynomial order as low as possible (Fig. A2c). Thus, the front location could be uncovered at the depths occupied by the three layers of central waters (CW).

2.5 Water masses distribution

An optimum multiparameter method (OMP, Karstensen and Tomczak (1998)) was used to quantify the contribution to the observations of the following water types: upper and lower North Atlantic Deep Water (UNADW and LNADW); Labrador Sea Water (LSW); Mediterranean Water (MW); AAIW; Subpolar Mode Water (SPMW); SACW of $12°C$ and $18°C$ (SACW12 and SACW18); ENACW of $12°C$ and $15°C$ (ENACW12 and ENACW15); and Madeira Mode Water (MMW). The hydrographic variables used for the analysis were θ, S_P, SiO_4H_4, and NO ($NO = O_2 + R_N \cdot NO_3^-$, where $R_N = 1.4$ is the stoichiometric ratio of organic matter remineralization, Anderson and Sarmiento (1994)) (Broecker, 1974). The reference values of these variables at the source region of each water type were extracted from the literature (Pérez et al., 2001; Álvarez and Álvarez-Salgado, 2009; Lønborg and Álvarez-Salgado, 2014) and WOA13 (Locarnini et al., 2013; Zweng et al., 2013; Garcia et al., 2014a, b). A linear system of normalized and weighted equations for θ, S_P, SiO_4H_4, NO and mass conservation was solved to obtain the water type proportions in the observations. Considering the measurement error, the relative conservative nature and the variability of each variable, the weights assigned to the balance of SiO_4H_4, NO, θ and S_P were 1, 2, 10 and 10, respectively. A weight of 100 was imposed to the mass conservation equation assuming the mass is fully conserved. On the other hand, in order to solve this undetermined system of equations, the water types were grouped in a maximum of 4 according to oceanographic criteria. In this way the unknowns were reduced from 11 to 5 with the following groups of water types: 1) MW - LSW - UNADW – LNADW; 2) SPMW – AAIW - MW – LSW; 3) SACW12 - ENACW12 - SPMW - AAIW; 4) SACW18 - ENACW15 - SACW12 - ENACW12; and 5) MMW - SACW18 - ENACW15. Surface waters ($<100\,\mathrm{dbar}$) were excluded from the analysis due to their non-conservative behavior. This OMP with high determination coefficients ($R^2 > 0.97$) and low standard errors of the residuals of θ, S_P, SiO_4H_4, and NO reproduced realistically the thermohaline and chemical fields during FLUXES-I (Valiente et al., in prep.).

2.6 Inverse model setup

The lateral geostrophic velocities were calculated at the boundaries of the volume closed by hydrographic stations. Geostrophic velocities were referenced to $\gamma_n = 27.82\,\mathrm{kg\,m^{-3}}$ ($\sim 1333\,\mathrm{m}$, Fig. A3). As an initial guess, the velocities at the reference level were those estimated from the climatological summer mean provided by GLORYS.

An inverse box model (Wunsch, 1978) was then applied to estimate a set of unknowns based on the assumption of mass, salt and heat conservation within a closed volume. The unknowns in the system are an adjustment of the initial reference level velocities, an adjustment of Ekman transports and the freshwater flux. The reference level velocity field was then used to estimate the absolute water mass transport through each transect of the cruise (Martel and Wunsch, 1993; Paillet and Mercier, 1997; Ganachaud, 2003a; Machín et al., 2006; Pérez-Hernández et al., 2013; Hernández-Guerra et al., 2017; Fu et al., 2018; Burgoa et al., 2020).

The cruise was carried out over 25 days, a time lag large enough for the structures to evolve during the sampling. This time lag is not generally an issue that would introduce a relevant bias in the calculations; however, in this case we have a closed volume composed by four hydrographical legs, so trying to connect the eastern section with the northern one might introduce

a large bias in the observations and consequently in the geostrophic velocity field. Hence, to avoid any imbalances induced by the temporal evolution of the system, the volume is closed with land instead of with the eastern transect. To do so, WOA18 climatological nodes were used to extend the transects N and S eastward (green dots in Fig. A1), where the climatological summer mean of GLORYS was also included at the reference level. Therefore, the geostrophic velocities at the reference level were modified with the inversion in transects N, W and S, while in transect E those velocities kept their initial climatological summer mean values from GLORYS.

The model was made up of 8 layers bounded by the free surface and 8 isoneutrals (26.46, 26.85, 27.162, 27.40, 27.62, 27.82, 27.922 and 27.962 $\mathrm{kg\,m^{-3}}$), reproduced essentially from those defined by Ganachaud (2003a) for the North Atlantic Ocean (Fig. A3). The inverse model considered mass conservation and salinity anomaly conservation per layer and also over the whole water column (Ganachaud, 2003b). Heat anomaly was introduced only in the deepest layer where it was also considered conservative. Salinity and heat were added as anomalies to improve the conditioning of the model and reduce the linear dependency between equations (Ganachaud, 2003b). Therefore, the inverse model was composed of 19 equations (9 for mass conservation, 9 for salt anomaly conservation and 1 for heat anomaly conservation). Those equations were solved using a Gauss-Markov estimator for 69 unknowns, comprised of 65 reference level velocity adjustments, 3 unknowns for the Ekman transport adjustments (one per transect), and 1 unknown for the freshwater flux.

It was necessary to provide *a priori* the uncertainties related to the noise of the equations (R_{nn}) and the unknowns (R_{xx}) in order to solve this undetermined system. R_{nn} and R_{xx} values are compiled in Tab. A1. The noise of each equation depends on the layer thickness, on the density field, and on the variability of the velocity field (Ganachaud, 1999, 2003b; Machín et al., 2006). Thus, an analysis of the velocity variability was performed in the mean depths of the 8 layers. The velocity variance at each layer was estimated from summer months in the 25 years of GLORYS data. These variances were transformed into transport uncertainty values multiplying by density and the vertical area of the section involved (R_{nn} in Tab. A1). The uncertainty assigned to the total mass conservation equation was the sum of the uncertainties from the 8 mass conservation equations. The equations for salt and heat anomaly conservation depend on both the uncertainty of the mass transport, on the variance of these properties and, specifically, on the layer considered (Ganachaud, 1999; Machín, 2003). Therefore, the uncertainties for salt and heat anomaly equations were estimated as follows (Ganachaud, 1999; Machín, 2003): $R_{nn}(Cq) = a*var(C_q)*R_{nn}(mass(q))$ where $R_{nn}(Cq)$ was the uncertainty in the anomaly equation of the property (salt or heat anomaly); $var(C_q)$ was the variance of this property; a was a weighting factor (4 in the heat anomaly, 1000 in the salt anomaly and 10^6 in the total salt anomaly) and q was a given equation corresponding to a given layer. Then, these variability estimates were included in the inverse model as the *a priori* uncertainty on the noise of equations in terms of variances of mass, salt anomaly and heat anomaly transports.

The variance of the velocities in the reference level was used as a measure of the *a priori* uncertainty for these unknowns. These variances were also calculated from the summer months velocities provided by GLORYS (R_{xx} in Tab. A1).

The initial Ekman transports were estimated from the average wind stress during the days of the cruise. A 50% uncertainty was assigned to the initial estimate of Ekman transports, related to the errors in their measurements and to the variability of the wind stress. An uncertainty of 50 % of the initial value of the freshwater flux, which was 0.0935 Sv, was also considered (Ganachaud, 1999; Hernández-Guerra et al., 2005; Machín et al., 2006). Both the Ekman transports, the freshwater flux and

their uncertainties (R_{xx} in Tab. A1) were added to the inverse model in the shallowest layer for mass and salt anomaly, and also in the total mass transport and total salt anomaly transport equations.

Dianeutral transfers between layers were considered to be negligible as compared to other sources of lateral transports, so they were not included in the inversion. Furthermore, the inverse model works with information only from the box boundaries and cannot be used to provide any spatial details of dianeutral fluxes for a given interface between layers but just an average value for the whole interface (Burgoa et al., 2020).

The resulting absolute geostrophic velocity field allowed us to calculate transports of O_2 and inorganic nutrients. Those transports were obtained by multiplying their concentration times mass transports, so their concentrations were initially interpolated to the positions where the absolute geostrophic velocities were estimated.

3   RESULTS

3.1   Hydrography and water masses

The main water masses sampled during FLUXES-I were ENACW (merging MMW, ENACW15 and ENACW12) and SACW (SACW18 and SACW12) below the mixing layer and above 700 m; modified AAIW and MW from 700 up to 1700 m; and North Atlantic Deep Water (LSW and UNADW) below 1600 m (Zenk et al., 1991; Martínez-Marrero et al., 2008; Pastor et al., 2012) (Figs. A3, A4 and A5). $\Theta - S_A$ definitions proposed by Tomczak (1981) for the salty and warm ENACW and the fresh and cold SACW (straight lines in Fig. A4) were used to identify CW in all transects: the main water mass sampled in transects N and W was ENACW (~ 36.15 g kg^{-1} at 300 m), while SACW was dominant in transect S (~ 35.65 g kg^{-1} at 300 m). Both ENACW and SACW were registered along transect E. Water masses were also well defined at intermediate levels, with colder and fresher AAIW over warmer and saltier MW. MW was sampled mainly in transect N and at smaller proportions in the northern part of transects E and W, while AAIW was the main water mass recorded at transects S, E and W (Fig. A4).

Figure A3 presents the high resolution γ_n field once the XBTs were considered. The upper four layers transported surface waters (SW, first layer above 26.46 kg m^{-3}) and CW between 26.46 and 27.40 kg m^{-3}; intermediate waters (IW) flowed along the next three layers between 27.40 and 27.922 kg m^{-3}, while deep waters (DW) did so at the deepest layer below 27.922 kg m^{-3}.

The overall distributions of O_2, NO_3, PO_4 and SiO_4H_4 at CW were highly variable and closely related to the location of the different water masses. In transects N and W, where ENACW was dominant, the O_2 concentrations were higher than in transects S and E where SACW was found, with minimum O_2 values lower than 60 µmol kg^{-1} at 300 m (Fig. A6). In contrast, the concentrations of the three inorganic nutrients in these last two transects were higher than in transects N and W at CW levels, with concentrations around 27-30 µmol kg^{-1} for NO_3, 1.5-1.7 µmol kg^{-1} for PO_4, and 7.5-9.9 µmol kg^{-1} for SiO_4H_4 at 300 m depth (Figs. A6 and A7).

At IW, the O_2 distribution was quite uniform in all transects, presenting a slight increase with depth. With respect to inorganic nutrients, their concentrations at transect N were lower than at the remaining transects, which were occupied by a larger amount of AAIW. Indeed, the largest NO_3 and PO_4 concentrations were registered associated to AAIW around 1000 m in transects

S and E (Figs. A6 and A7). Finally, at the deepest layer, high concentrations of O_2 and inorganic nutrients were found. Specifically, the highest concentrations of SiO_4H_4 were recorded at this deepest layer.

The hydrological and biogeochemical characteristic of the water masses are summarized in Figures A8 and A9, where the relationships between *in situ* measurements of S_A, O_2, NO_3 and PO_4 are displayed. These property-property distributions might be used to define the characteristic values of the water masses in the domain (Emery, 2001). At CW, inverse tight relationships are obtained for NO_3 and PO_4 with S_A, while the relationship is direct and looser for O_2 with S_A. At IW, the relationships between NO_3 and PO_4 with S_A is much less defined, with a 'S'-like pattern. In all cases, the relationships between O_2 with NO_3 or PO_4 are rather tight and inverse.

The previous distributions are presented from a large-scale perspective. A second reading on the dataset might be performed emphasizing the role played by mesoscalar structures. For instance, an intrathermocline anticyclonic eddy centered in station 4 was detected in Θ, S_A, O_2, NO_3 and PO_4 (Figs. A5, A6 and A7). On the other side, the CVF was also detected in transects S and E as a sharp transition in all properties (Figs. A5, A6 and A7). In particular, O_2 presented two remarkable minimum values of $60\ \mu mol\,kg^{-1}$ between 100 and 150 m when the frontal area was crossed (Fig. A6). Just below these O_2 minima, the local maxima of NO_3, PO_4 and SiO_4H_4 were recorded (Figs. A6 and A7).

3.2   Cape Verde Front

The CVF has historically been defined at only one depth, where the isohaline 36 (or $36.15\ g\,kg^{-1}$, Burgoa et al. (2020)) intersects the isobath 150 m (Zenk et al., 1991). Following that definition, the CVF could be located during FLUXES-I between stations 23 and 24 in transect S, where $\Delta S_A > 0.70\ g\,kg^{-1}$ and $\Delta\Theta > 1.92\ ^\circ C$ were observed between both sides of the front; CVF was also detected between stations 33 and 34 in transect E with lower $\Delta S_A > 0.30\ g\,kg^{-1}$ and $\Delta\Theta > 1.10\ ^\circ C$ values (Fig. A5).

The method developed in this manuscript to estimate the vertical location of the front depicted a complex spatial distribution (Fig. A10). CVF is represented by several isohalines associated to specific depths. These isohalines unveil that the front was almost completely vertical in transect E, while at the W-S corner it presented a notable slope with its surface end located south of its deep end. Hence, the front was oriented from north-east to south-west at near surface layers, while it presented a roughly east-west orientation at 698 m depth (Figure A10a). On the other hand, the CVF location presented with this methodology is indicated along the transects (pink lines), revealing a remarkable match with the distributions of the maximum contributions of ENACW (MMW+ENACW15+ENACW12) and SACW (SACW18+SACW12) estimated with the OMP (Figs. A10b and c).

3.3   Inverse model solution

The inverse model provided absolute geostrophic velocities for transects N, W and S, extended to the coast with WOA nodes. Mass transports are then evaluated to estimate the mass imbalance within the closed box. Figure A11 presents the mass transports accumulated along transects N, W and S, grouped by different water levels (upper panel) and also the transports integrated per layer and transect (lower panel). Note that positive/negative values represent outward/inward transports from/to the closed box (1 Sv=$10^9\ kg\,s^{-1}$). The mass transport imbalance in every water level was roughly zero once it was accumulated along

the box, indicating that the mass was highly conserved (Fig. A11a). An imbalance was observed in the net transport mainly associated with the first and third layers (black line in Fig. A11b), likely related to mesoscale structures under-sampled during the cruise.

Large transports are obtained in the entire water column. In the two shallowest layers the mass exchange is basically from north and south to the west, carrying some 3.4 Sv. In the third and fourth layers, transports continued entering from the south, while transports reversed on transects N and W, flowing a total of some 1 Sv. At IW levels, the estimated transports were moderately high and northward, with more than 3 Sv that entered through transects W and S. At DW levels, the integrated mass transports are around 1 Sv, maintaining IW levels' scheme.

The results obtained from the inversion are compared with two independent databases: transports from altimetry and transports from the numerical model GLORYS (Fig. A12). These transports are calculated by multiplying the velocity at surface times the vertical area covered by the first layer in the inverse model. Accordingly, in the case of the inverse model we have used the accumulated mass transports in the first layer. The overall transport structure is rather similar for all three cases, in particular between the inverse model and the altimetry. GLORYS might not be recovering the mesoscale signal and its low response to this variability is likely deviating it from the other two databases. In all cases, the final imbalance is quite similar and about 1.5-2 Sv.

3.4 Geostrophic velocity

The previous result is now applied to present the geostrophic velocities along the three transects developed to perform the inverse model. Figure A13 displays the absolute velocity field perpendicular to each transect with a geographic criteria (positive velocities are northward and eastward). The absolute velocity field might be described as alternating vertical cells with velocities in the range from -0.25 to 0.25 $\mathrm{m\,s^{-1}}$; the largest velocities are mainly found in the upper 200-300 m depth.

This velocity field helps to identify several mesoscale features captured during the cruise. Besides the intrathermocline anticyclonic eddy located between stations 3 and 5, another cyclonic eddy was centered between stations 5 and 7, next to the first eddy. Transect N was also crossed by a second anticyclonic eddy between stations 9 and 12. The main mesoscale structures sampled in transect W were a meander between stations 15 and 18 and also an intrusion found between stations 18 and 19, which actually entered the box through corner W-S. A second part of this intrusion is observed at transect S, where it entered the box between stations 19 and 20 and left between stations 20 and 21. From stations 22 to 26, some additional meandering was observed along transect S. A cyclonic eddy had a notable negative velocity in the middle part of the transect S centered at station 27.

3.5 Inorganic nutrient and O_2 transports

The transports (integrated per water level and transect) for O_2, NO_3, PO_4 and SiO_4H_4 are presented in Figure A14 and compiled in Table A2. At IW and DW levels, the transports for all properties are nearly balanced and may be described as a net northward transport with contributions from the western and southern transects.

However, the transports at SW and CW levels present an imbalanced distribution that can not be fully related to imbalances in the mass transports, as mass transports are nearly balanced at those water levels. Transports present a distribution where O_2 enters the box through transects N and S; a lower amount of O_2 leaves the box through transect W revealing a net O_2 decay within the box. The highest O_2 transports are obtained at SW levels, as a combined effect of large velocities and high O_2 concentration at the photosynthetic layer in contact with the atmosphere. Finally, the pattern in the transports distribution is quite the same for NO_3, PO_4 and SiO_4H_4: nutrients leave the domain through transects N, W and S, with a tiny amount getting in the box through transect N at SW and CW. The lowest transports for inorganic nutrients are obtained at the SW layer, as a consequence of nutrient depletion within the photic layer, while the highest transports are observed at CW and IW levels. A large imbalance is obtained at CW levels, providing a net nutrient increase within the box at CW levels.

Biogeochemical budgets can be obtained for the entire water column, once we have produced the net lateral transports of O_2 and inorganic nutrients (Table A2). To do so, first we still need to estimate the O_2 exchange between the sea surface and the atmosphere. We have proceeded as documented by Wanninkhof (2014), using an average wind speed for the whole domain (U, m s^{-1}) and the Schmidt number (Sc) for O_2 to estimate the gas transfer velocity (k, cm h^{-1}) as $k = 0.251 < U^2 > (Sc/660)^{-0.5}$. Then, we estimated the average Apparent Oxygen Utilization (AOU), and estimate the O_2 transport from the sea surface to the atmosphere as $F = -k\overline{AOU}A/1000$, where A is the surface area of the domain (m^2). These calculations provide an O_2 export to the atmosphere of 113.54 kmol s^{-1}. This number indicates that the total O_2 consumption within the box is 163.8 kmol s^{-1}, as the lateral transport integrated for the whole sampled water column was -277.34 kmol s^{-1}. On the other hand, the inorganic nutrient positive balances indicate that the domain is producing inorganic nutrients likely as a consequence of remineralization below the photic layer; the nutrient import from the atmosphere are considered negligible as compared to their lateral transports, according to climatological values reported by Fernández-Castro et al. (2019). Hence, this domain would be acting as an heterotrophic box, as revealed by the net oxygen consumption, with remineralization of N, P and Si below the photic layer.

4 DISCUSSION

We have presented the dynamics related to the water masses and their O_2 and inorganic nutrient content in the transition between the eastern NASG and the NATG during summer 2017. The water masses distribution in the CVFZ during FLUXES-I is consistent with that documented before (Hernández-Guerra et al., 2005; Pastor et al., 2012; Peña-Izquierdo et al., 2012; Burgoa et al., 2020): a latitudinal change between ENACW and SACW below the mixing layer and above 700 m was detected from north to south (Pelegrí et al., 2017), while a second latitudinal transition was observed at IW between AAIW and MW from south to north (Zenk et al., 1991), being AAIW the dominant water mass. The characteristic of these water masses are conditioned by their origin and path followed in their way to the CVB. While transects N and S present well defined water masses, transects W and E reflect a water masses transition between transects N and S. The large variability registered at SW and CW levels is related to the position of the CVF, with the proximity of the CUF north of the domain and with the meso- and sub-mesoscale structures associated with these two frontal systems, as the upwelling filaments off Cape Blanc (Meunier et al.,

2012; Lovecchio et al., 2018; Appen et al., 2020). ENACW and SACW property distributions presented in Figure A8 compare well with those reported by Pastor et al. (2008) and Pelegrí and Benazzouz (2015b). At IW levels, the variability is mainly related to the AAIW flowing northward to the Canary Islands basin (Machín and Pelegrí, 2009; Machín et al., 2010). The shadow zone documented by Kawase and Sarmiento (1985) and the development of an oxygen minimum zone (OMZ) within

5   CW and IW levels was centered in transect S between 100 and 800 m depth with its core around 400 m between isoneutrals 27.1 and 27.3 $kg\,m^{-3}$ (Karstensen et al., 2008; Brandt et al., 2015; Thomsen et al., 2019). That distribution matches well with the one provided by Peña-Izquierdo et al. (2015) with high concentrations of NO_3 and PO_4.

    A major contribution from this manuscript is the development of an extended version for the classical methodology applied to locate the CVF. Following the definitions for SACW and ENACW reported by Tomczak (1981) and the interpretation of

10   the CVFZ by Zenk et al. (1991), the front 3D structure from 150 to 650 m depth has been produced combining *in situ* and GLORYS data (Fig. A10). Fist of all, we would like to highlight the consistency between the results produced from the *in situ* observations when compared to the results from the GLORYS model. The front spatial disposition reveals that the CVF is a complex meandering front with several associated mesoscale features, showing a variable geographical orientation at different depths (Barton, 1987; Martínez-Marrero et al., 2008; Pastor et al., 2008, 2012). The vertical distribution of the CVF enables

15   the interpretation of the imbalances in lateral transports of mass, O_2 and inorganic nutrients at both sides of the front (Tab. A3). The predominance/lack of SACW/ENACW in transect S suggests that the CVF may be functioning as a barrier against lateral transports across the front. The CVF also influenced its adjacent waters, as observed for example in the minima of O_2 and the maxima of NO_3 and PO_4 sampled just below 150 m in the tropical side of the front, that might be indicating a local remineralization (Fig. A6) (Thomsen et al., 2019).

20   The main limitation in the present analyzes were related to the high relative importance of mesoscale features in the domain. These features modify the thermohaline field with an intensity capable of inducing transports within the same order of magnitude as those related to the large-scale circulation (Volkov et al., 2008; Zhang et al., 2014). On the one side, if the mesoscale field is under-sampled, it might induce large imbalances when quantifying the large-scale transports. On the other side, the important dynamics associated with the mesoscale might also produce a lack of synopticity when the sampling takes longer

25   than 15-20 days. These two effects might be responsible of the main limitations found in the dataset, as mesoscalar structures were observed in almost all hydrographic sections. In turn, mesoscale structures impact on the physical-chemical variables in the domain, that might end up significantly altered (Appen et al., 2020). A second limitation could be the absence of diapycnal transfers in the model. The imbalances diagnosed for the SW and CW would be reduced if a downwelling in the upper 300 m developed as a consequence of the upwelling relaxation during the cruise dates.

30   The velocity field has a direct implication in the exchange of O_2 and inorganic nutrients at intermediate and deep water levels. The net balanced northward transport carries some 827 $kmol\,s^{-1}$ of O_2, 112 $kmol\,s^{-1}$ of NO_3, 7.3 $kmol\,s^{-1}$ of PO_4 and 100 $kmol\,s^{-1}$ of SiO_4H_4. These values are well above the horizontal advection estimated from climatological data reported by Fernández-Castro et al. (2019) at intermediate and deep levels. However, the net horizontal transports presented in both analyses have very small values in intermediate and deep waters.

On the other hand, at surface and central levels the role played by biogeochemical processes also needs to be considered to outline the full picture of the processes forcing the variability in the O_2 and inorganic nutrients transports. A westward imbalanced transport of O_2 is observed at SW and CW levels, with a deficit of some $368\,\mathrm{kmol\,s^{-1}}$ related to the lower O_2 concentration in the outflowing as compared to the inflowing waters (Fernández-Castro et al., 2019). With respect to nutrients at these levels, the domain acts as a source with net outward transports through the three transects of some $125\,\mathrm{kmol\,s^{-1}}$ for NO_3, $8\,\mathrm{kmol\,s^{-1}}$ for PO_4 and $52\,\mathrm{kmol\,s^{-1}}$ for SiO_4H_4. The western section presents the highest outward transports for the three nutrients at SW and CW as in Fernández-Castro et al. (2019); our transports, however, are much larger than the climatological values provided by these authors. The calculations performed for the whole box, where the O_2 export to the atmosphere was considered, somehow define a pattern for the offshore export of inorganic nutrients as a consequence of O_2 consumption followed by nutrient remineralization below the photic layer. In this case, we would not expect the result to fit within the Redfield ratio as we are working with the whole box instead of differentiating between the surface layer (where oxygen production and nutrient consumption dominate) and the layers below (where net oxygen consumption and inorganic nutrients mineralization occurs). To do so, we would need to deal separately with the surface layer and estimate the role played by vertical advection and turbulence, an approach beyond the scope of this study.

Despite the eastern section was not part of the inverse model, it still may provide insights about the transports within the domain in a location quite close to the coastal upwelling (Figure A15). Mass transports indicate eastward transport at SW, CW and DW levels, while at IW levels the transports reverse westward. Transports related to O_2 and inorganic nutrients reflect a similar pattern. O_2 transports are close to zero at SW and CW levels, likely as a result of the high relative importance of the OMZ in this eastern section. Nutrients at SW level present low onshore transports, while their transports increase at CW levels. At IW and DW levels, a straight relationship is also observed for O_2 and inorganic nutrients when compared with the mass transports pattern. Hence, at this eastern section it seems that the physical forcing has been the dominating factor to explain the variability in the transports.

Finally, the development of a frontal zone provides the opportunity to perform the transports analysis at both sides of the front, in the tropical and subtropical domains within CW levels (Tab. A3 and Fig. A16). The mass transport imbalance is less than 1 Sv in both sides of the front. The pattern associated with transports is consistent with a south-westward transport in the subtropical side and a westward transport in the tropical domain, consistent with previous authors as Pastor et al. (2008). Once the O_2 and inorganic nutrient transports are estimated at both sides, their behavior is quite similar with a net O_2 decay and a net increase of inorganic nutrients. The main difference between both sides is related to the transports of O_2, which is lower in the tropical side, about a half of the subtropical value, presumably related to the larger extension of the OMZ in this particular area.

5 CONCLUSIONS

In summary, the circulation in the transition zone between the coastal upwelling and the interior ocean, in the vicinity of the Cape Verde Front is described as a westward flow at surface and central levels, at both the tropical and subtropical sides of

the front, transporting about 3.76 Sv. Below, at intermediate levels, the circulation is markedly northward carrying about 3 Sv. Mesoscale features constitute a main source of variability in the circulation at these water levels. On the other hand, the Cape Verde Front has been featured from 100 to 700 m depth in the whole domain sampled; it presents a large meandering structure with an orientation varying with depth. Finally, the O_2 and inorganic nutrient transports at central levels are conditioned by

5   biogeochemical processes with a decrease of O_2 and an increase of inorganic nutrients. At intermediate levels, the variability in the O_2 and inorganic nutrient transports are highly conditioned by physical factors. Once the O_2 export to the atmosphere is accounted for, the domain has revealed as an heterotrophic system due to O_2 consumption, with a remineralization of inorganic nutrients.

Competing interests.   The authors declare that they have no conflict of interest.

10   *Acknowledgements.*   This work has been done thanks to the project FLUXES (CTM2015-69392-C3-3-R), funded by the Spanish National Research Program and the European Regional Development Fund (MINECO/FEDER). Furthermore, this research has been financially supported by on-going project E-IMPACT (PID2019-109084RB-C2). Currently, Nadia Burgoa is working on her PhD, with a fellowship funded by the Spanish Ministry of Economy and Competitiveness.
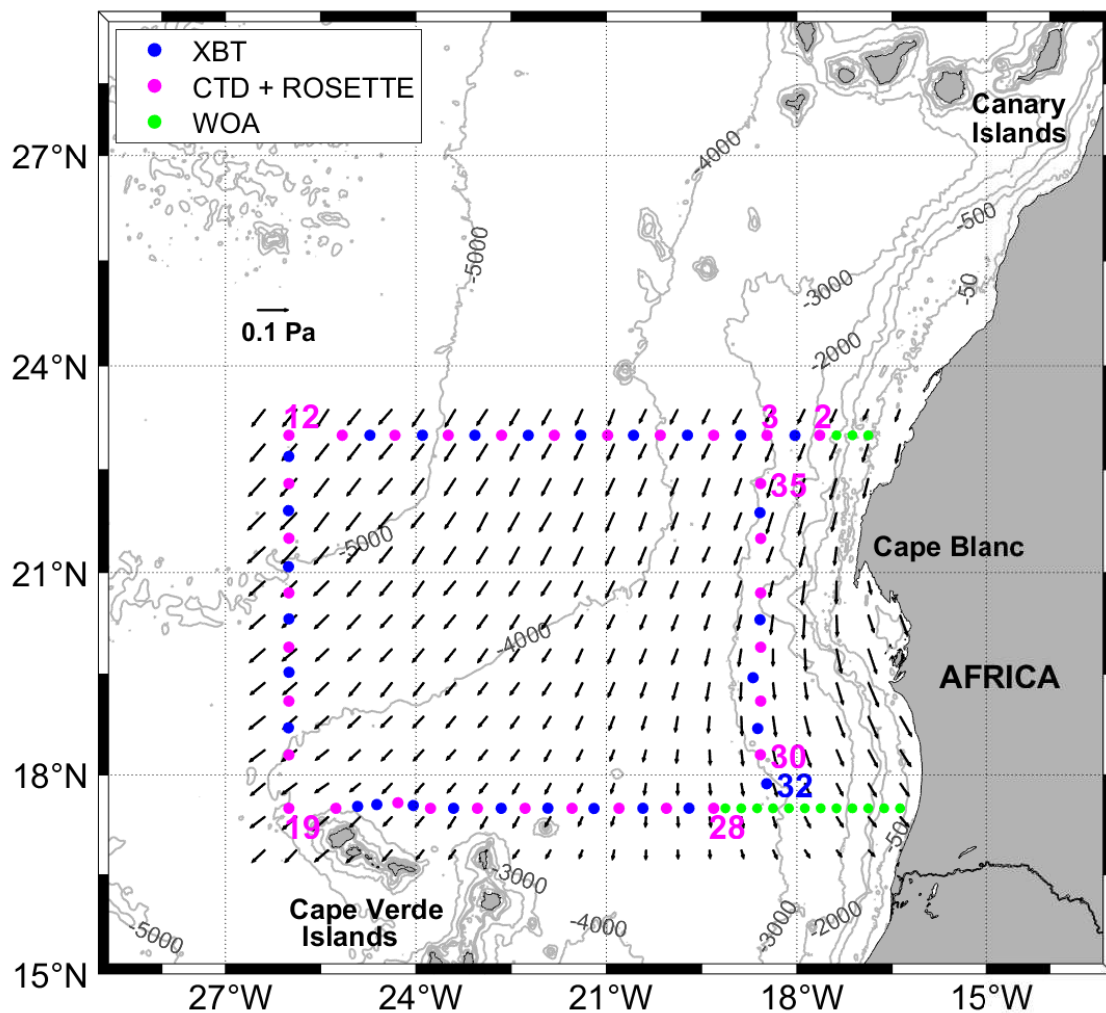
Figure A1. CTD-rosette sampling stations (pink dots) and XBT (blue dots) during FLUXES-I cruise. WOA stations are represented with green dots. Time-averaged wind stress during the cruise is also represented with the inset arrow denoting the scale (shown with half of the original spatial resolution).
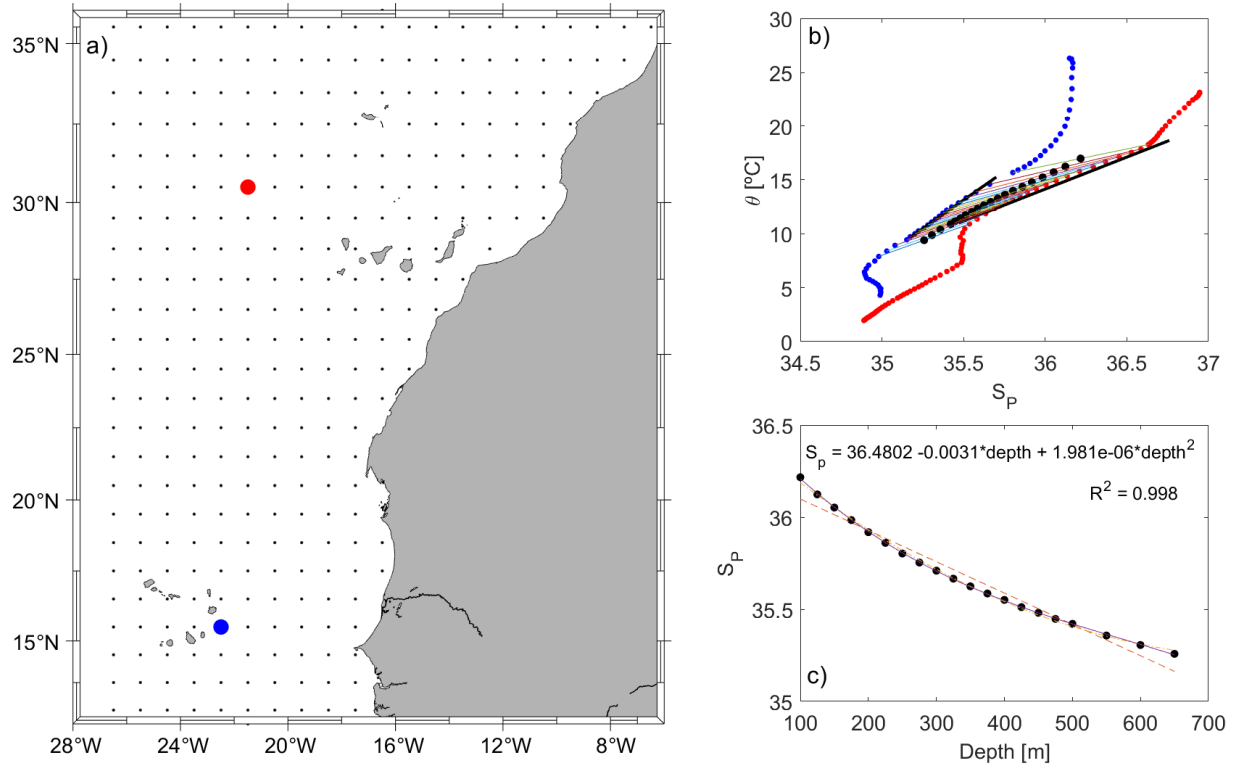
Figure A2. a) Map with the two selected WOA stations in ENACW (red) and SACW (blue) domains. b) TS diagram with the average salinity for each depth (in the range 100-650m) in black dots between the profiles of northern and southern WOA stations. Observations at the same depths are connected by a straight line. c) Linear, quadratic and cubic fits for depth versus salinity with the quadratic fit equation .
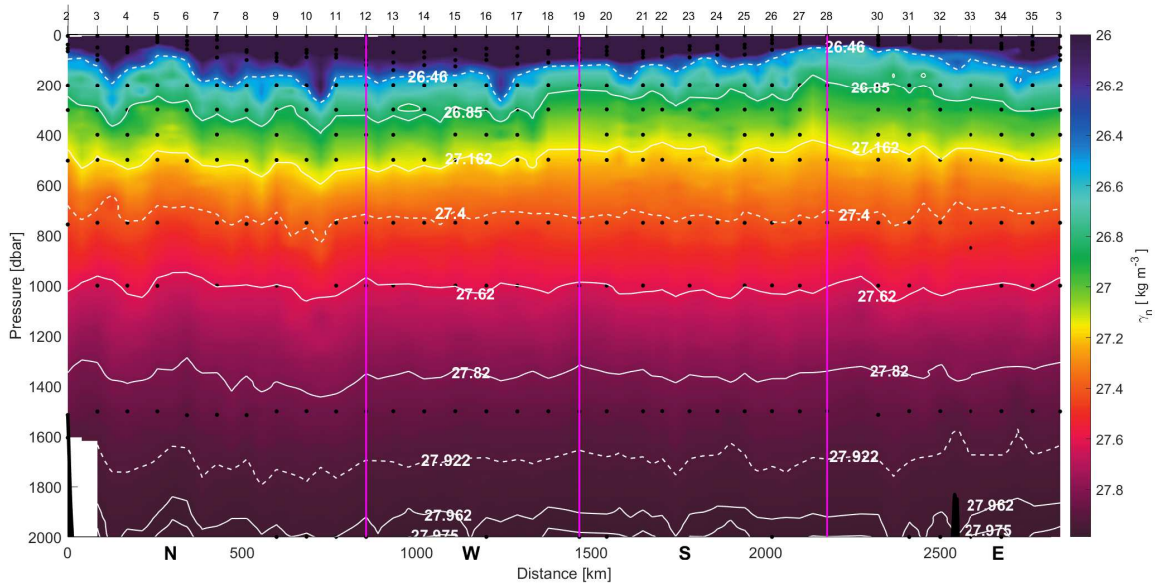
Figure A3. γ_n vertical section during FLUXES-I cruise produced with the CTD-XBT merged dataset. White dashed isoneutrals limit the different water type layers. The direction chosen for the representation of the transects is the course of the vessel. Distance is calculated with respect to the first station (2). The section is divided as follows: transect N from east to west (from station 2 to 12), transect W from north to south (from station 12 to 19), transect S from west to east (from stations 19 to 28) and transect E from south to north (from 28 to 3). The N/W, W/S and S/E corners are indicated with three vertical pink lines at stations 12, 19 and 28, respectively. The sampling points of dissolved oxygen and inorganic nutrients used in this work are represented in black dots.
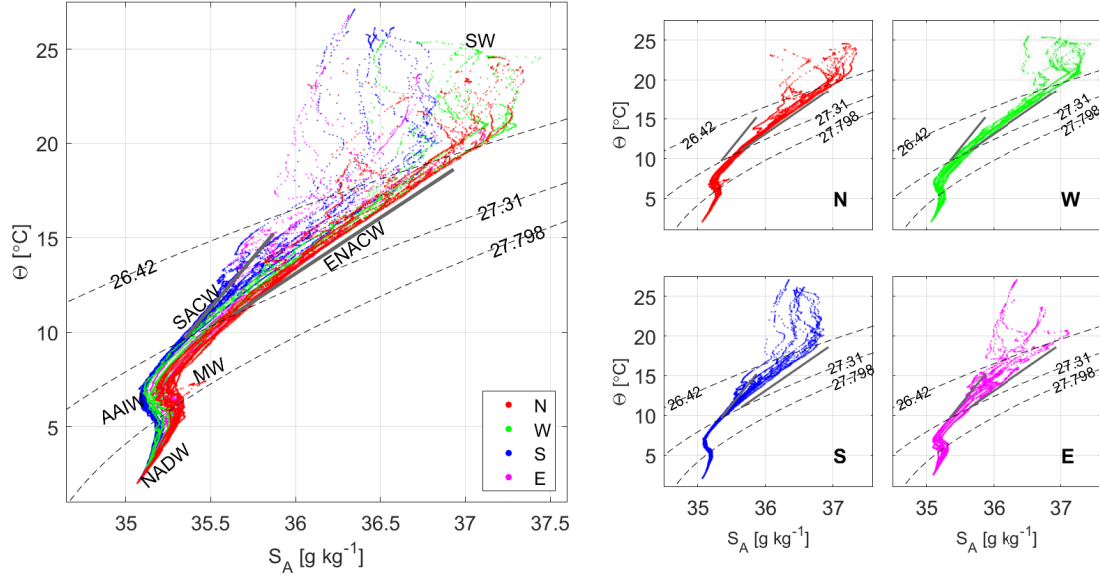
Figure A4. $\Theta - S_A$ diagrams during FLUXES-I cruise. The different water masses at northern (N, red dots), western (W, green dots), southern (S, blue dots) and eastern (E, pink dots) transects at surface waters (SW), North Atlantic Central Water (ENACW), South Atlantic Central Water (SACW), modified Antarctic Intermediate Water (AAIW), Mediterranean Water (MW) and North Atlantic Deep Water (NADW). Potential density anomaly contours (gray dashed lines) equivalent to 26.46, 27.4 and 27.922 $\mathrm{kg\,m^{-3}}$ isoneutrals delimit the surface, central, intermediate and deep water levels. Straight lines represent the $\Theta - S_A$ relationship for ENACW and SACW equivalent to that proposed by Tomczak (1981).
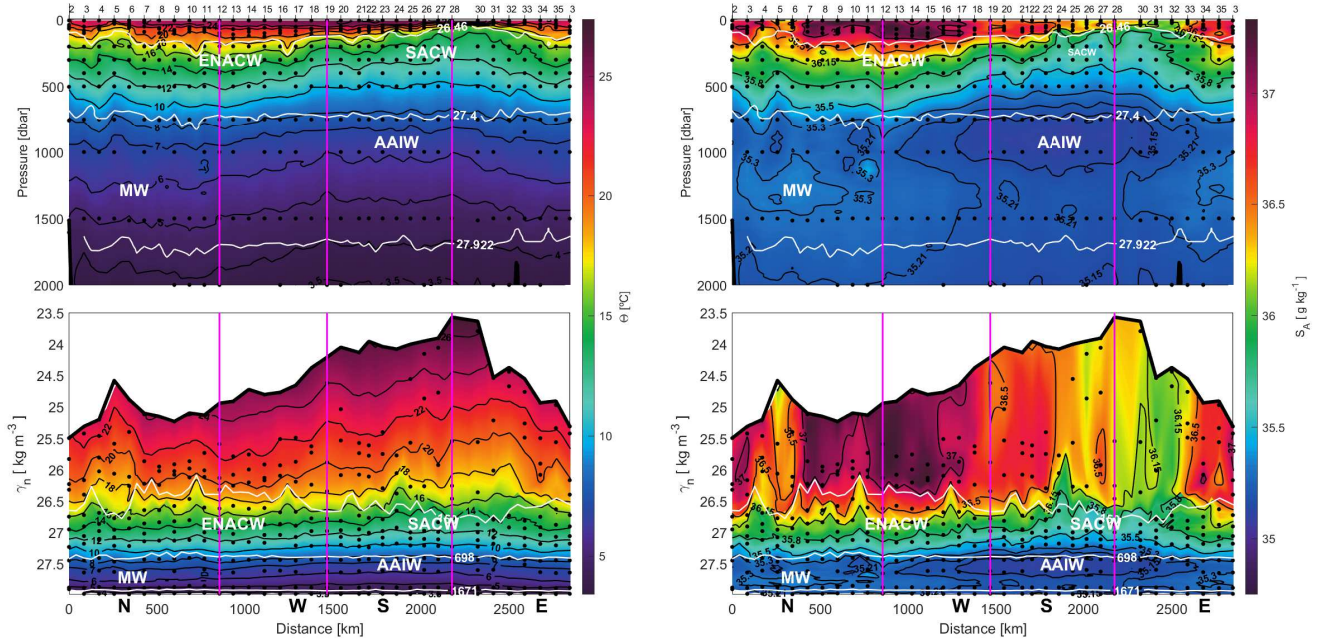
Figure A5. Sections of Θ (left) and S_A (right) with respect to depth (upper line) and γ_n (lower line) during FLUXES-I cruise. The direction chosen for the representation is the same as in Fig. A3. The N/W, W/S and S/E corners are indicated with three vertical pink lines at stations 12, 19 and 28, respectively. In depth sections, the isoneutrals which delimit the surface, central, intermediate and deep water are represented by white contours. In γ_n sections, the depths of 150, 698 and 1671 m are also shown. The sampling points of dissolved oxygen and inorganic nutrients used in this work are represented in black dots. Sections are estimated only with the CTD-XBT merged dataset.
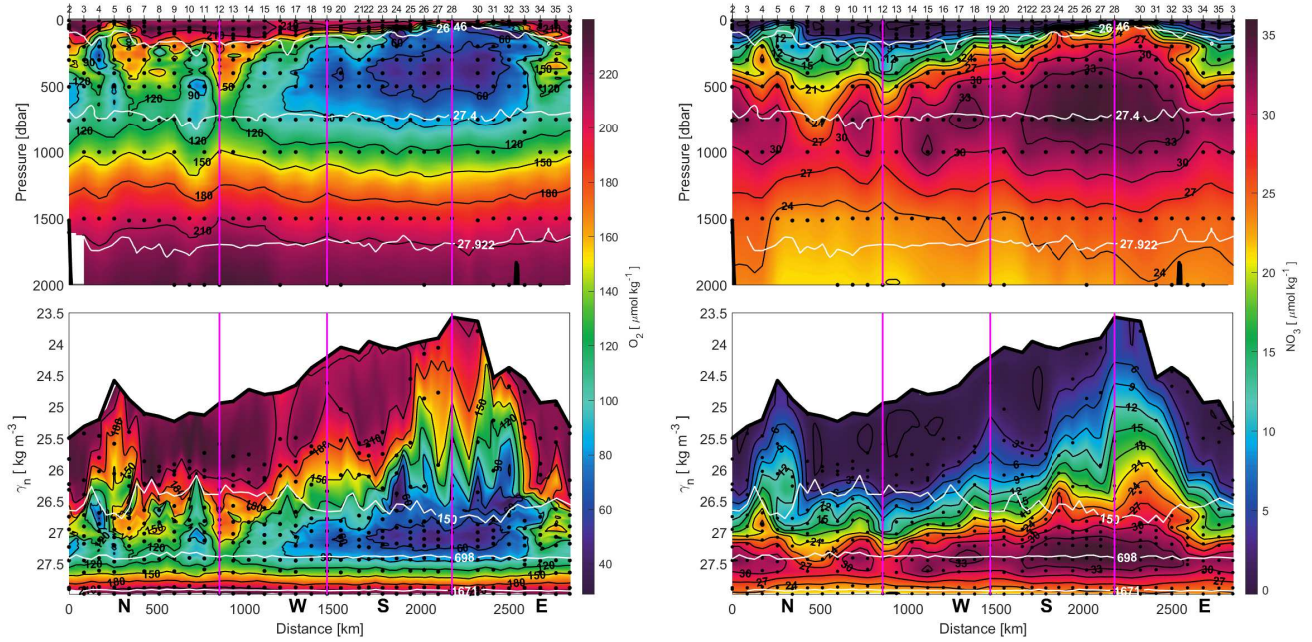
Figure A6. Sections of O_2 (left) and NO_3 (right) with respect to depth (upper line) and γ_n (lower line) during FLUXES-I cruise. The direction chosen for the representation is the same as in Fig. A3. The N/W, W/S and S/E corners are indicated with three vertical pink lines at stations 12, 19 and 28, respectively. In depth sections, the isoneutrals which delimit the surface, central, intermediate and deep water are represented by white contours. In γ_n sections, the depths of 150, 698 and 1671 m are also shown. The sampling points of O_2 and NO_3 used in this work are represented in black dots.
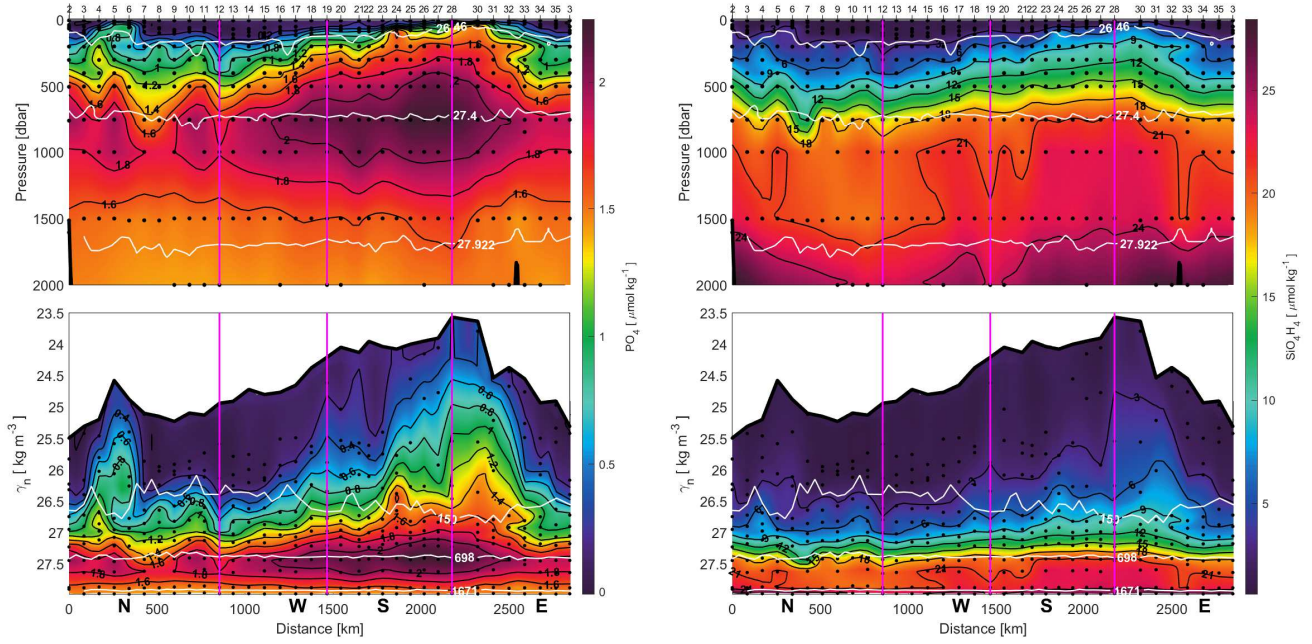
Figure A7. Sections of PO_4 (left) and SiO_4H_4 (right) with respect to depth (upper line) and γ_n (lower line) during FLUXES-I cruise. The direction chosen for the representation is the same as in Fig. A3. The N/W, W/S and S/E corners are indicated with three vertical pink lines at stations 12, 19 and 28, respectively. In depth sections, the isoneutrals which delimit the surface, central, intermediate and deep water are represented by white contours. In γ_n sections, the depths of 150, 698 and 1671 m are also shown. The sampling points of PO_4 and SiO_4H_4 used in this work are represented in black dots.
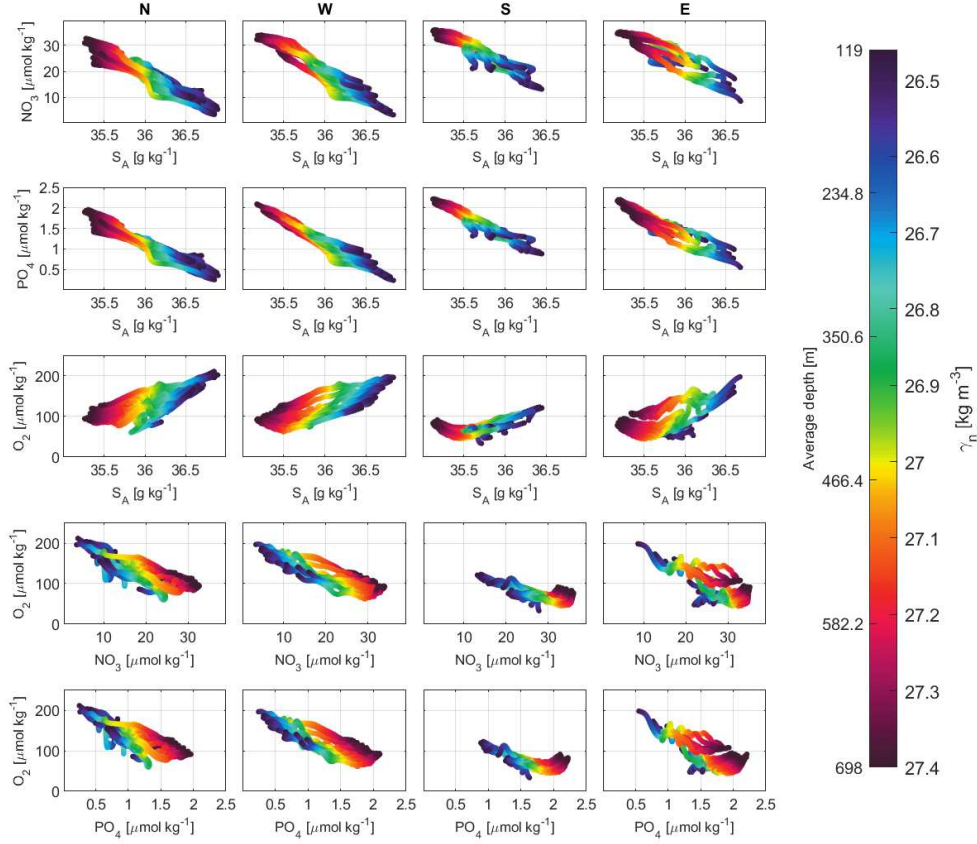
Figure A8. Scatter plots of *in situ* observations of NO_3, PO_4 and O_2 ($\mu mol\,kg^{-1}$) with respect to S_A and γ_n (in colour with an approximate scale of the average depths) in transects north (N, first column), west (W, second column), south (S, third column) and east (E, fourth column) for CW layers in first, second and third line. In fourth and fifth lines, scatter plots of NO_3-O_2 and PO_4-O_2 in 4 transects and also for CW layers.
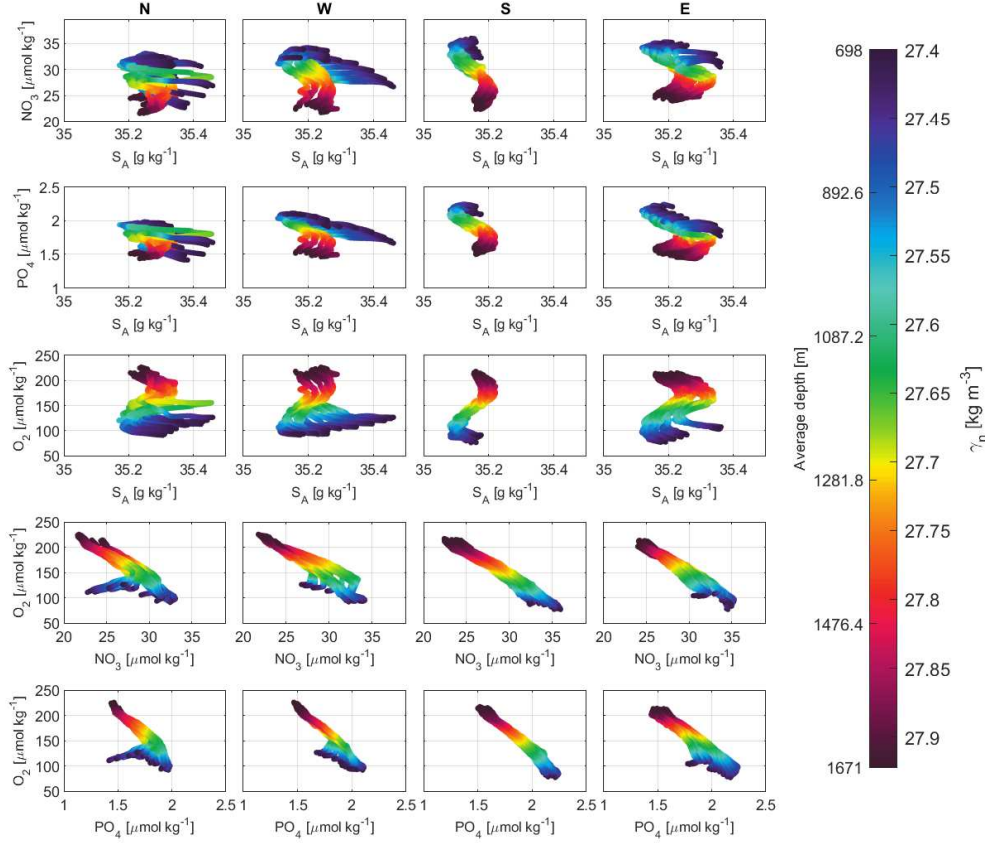
Figure A9. Scatter plots of *in situ* observations of NO_3 and PO_4 and O_2 in units of $\mu mol\,kg^{-1}$ with respect to S_A and γ_n (in colour with an approximate scale of the average depths) in transects north (N, first column), west (W, second column), south (S, third column) and east (E, fourth column) for IW layers in first, second and third line. In fourth and fifth lines, scatter plots of NO_3-O_2 and PO_4-O_2 in 4 transects and also for IW layers.
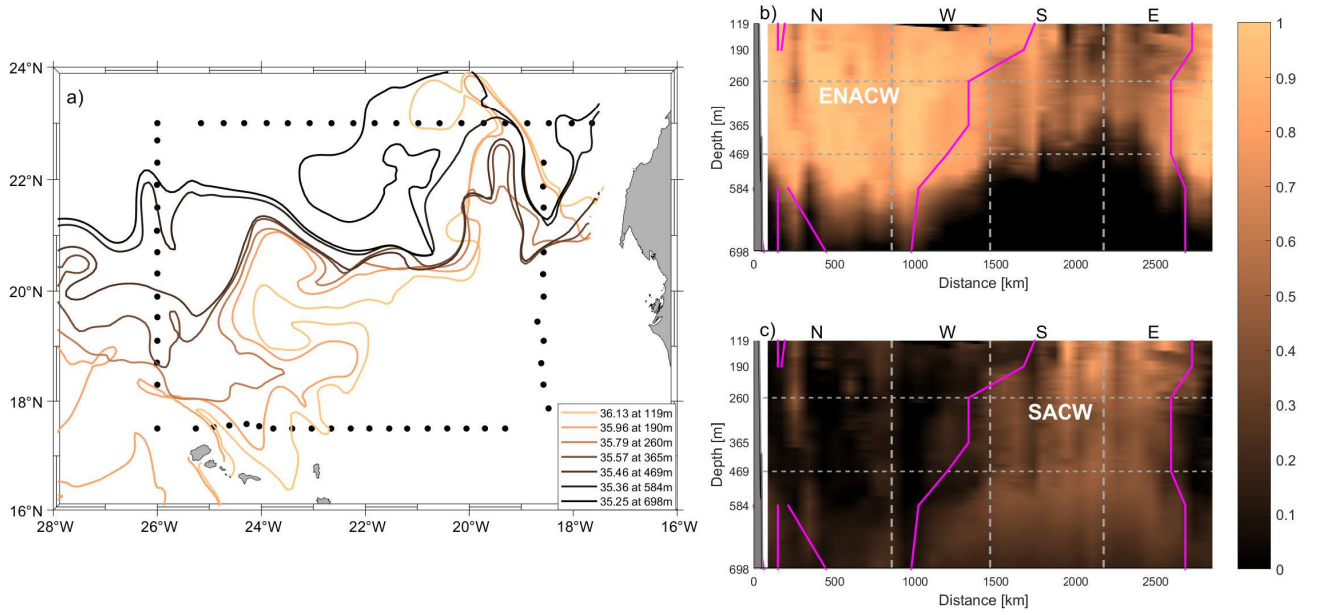
Figure A10. a) Location of the front at the isohalines 36.07, 35.88, 35.67, 35.43, 35.31, 35.2 and 35.08, corresponding to average depths of 119, 190, 260, 365, 469, 584 and 698 m equivalent to 26.46, 26.63, 26.85, 26.98, 27.162, 27.28 and 27.40 $\mathrm{kg\,m^{-3}}$. Vertical sections of the three layers of CW with the percentages of ENACW (b) and SACW (c), and the front location superimposed by pink lines. The direction chosen for the representation is the same as in Fig. A3. The N/W, W/S and S/E corners are indicated with three vertical grey dashed lines. Three layers are also separated by two horizontal grey dashed lines.
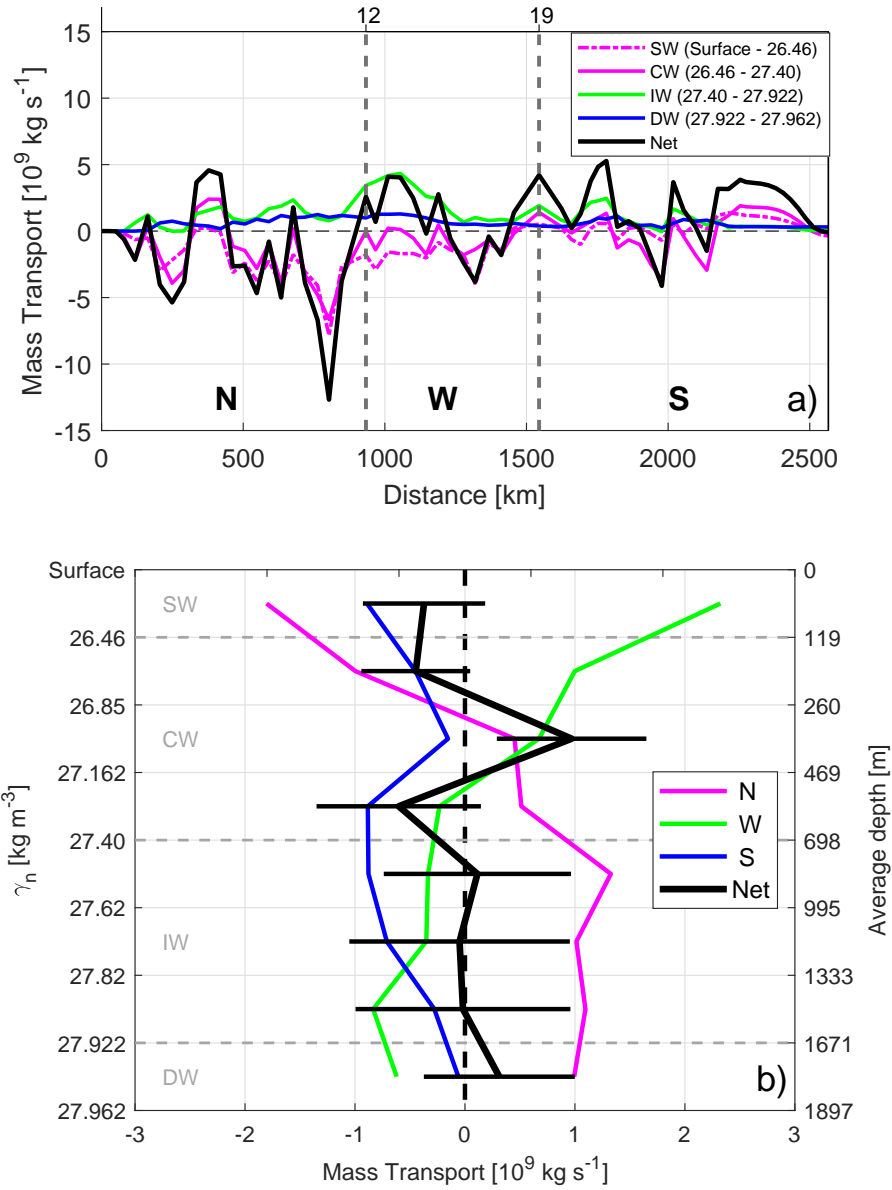
Figure A11. a) Accumulated mass transports per SW, CW, IW and DW levels and b) mass transports integrated per transect at north, west, and south, estimated by the inverse model during FLUXES-I cruise (including WOA stations in transects N and S). Negative/positive values indicate inward/outward transports in both plots. Mass conservation in the whole domain closed to coast is shown by the black line. The N/W and W/S corners are indicated with vertical dashed lines at stations 12 and 19 in the accumulated mass transports (a). The horizontal bars in each layer represented in the net mass transport are the errors estimated by the inverse model (b).
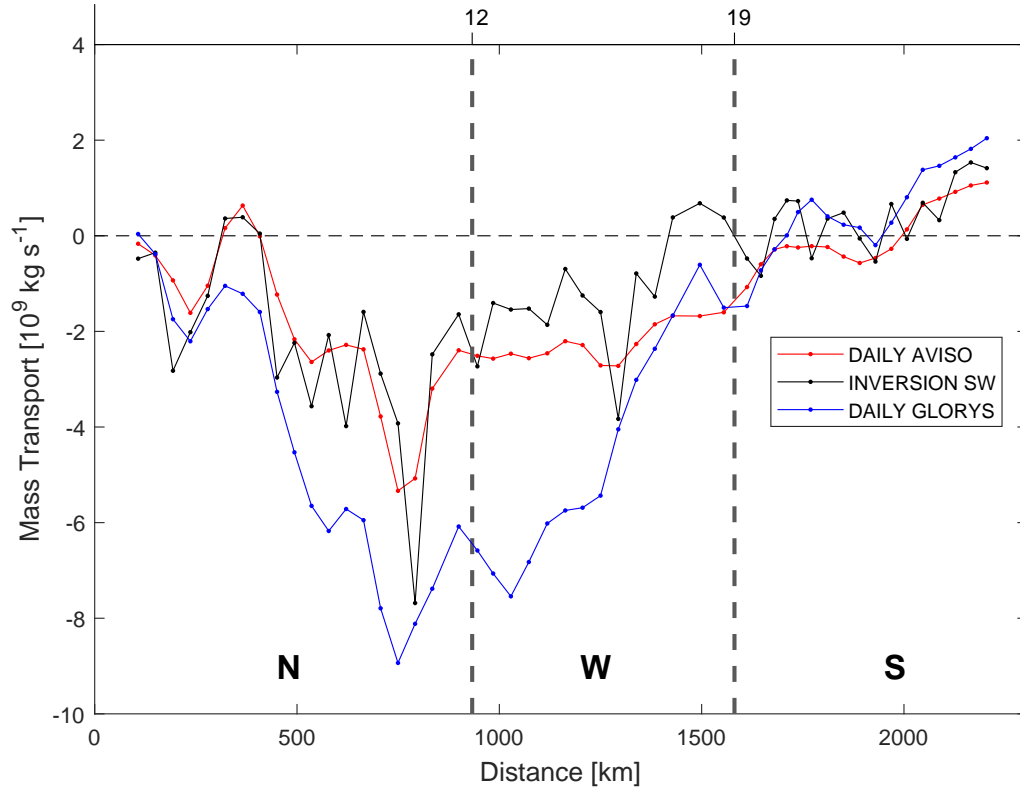
Figure A12. Accumulated mass transports in the first layer of SW estimated along transects N, W and S (without WOA stations) with altimetry's derived geostrophy (red line), inversion (with GLORYS' as reference velocities, black line) and GLORYS' field (blue line). Negative/positive values indicate inward/outward transports as in Fig. A11. The N/W and W/S corners (at stations 12 and 19) are indicated with vertical dashed lines.
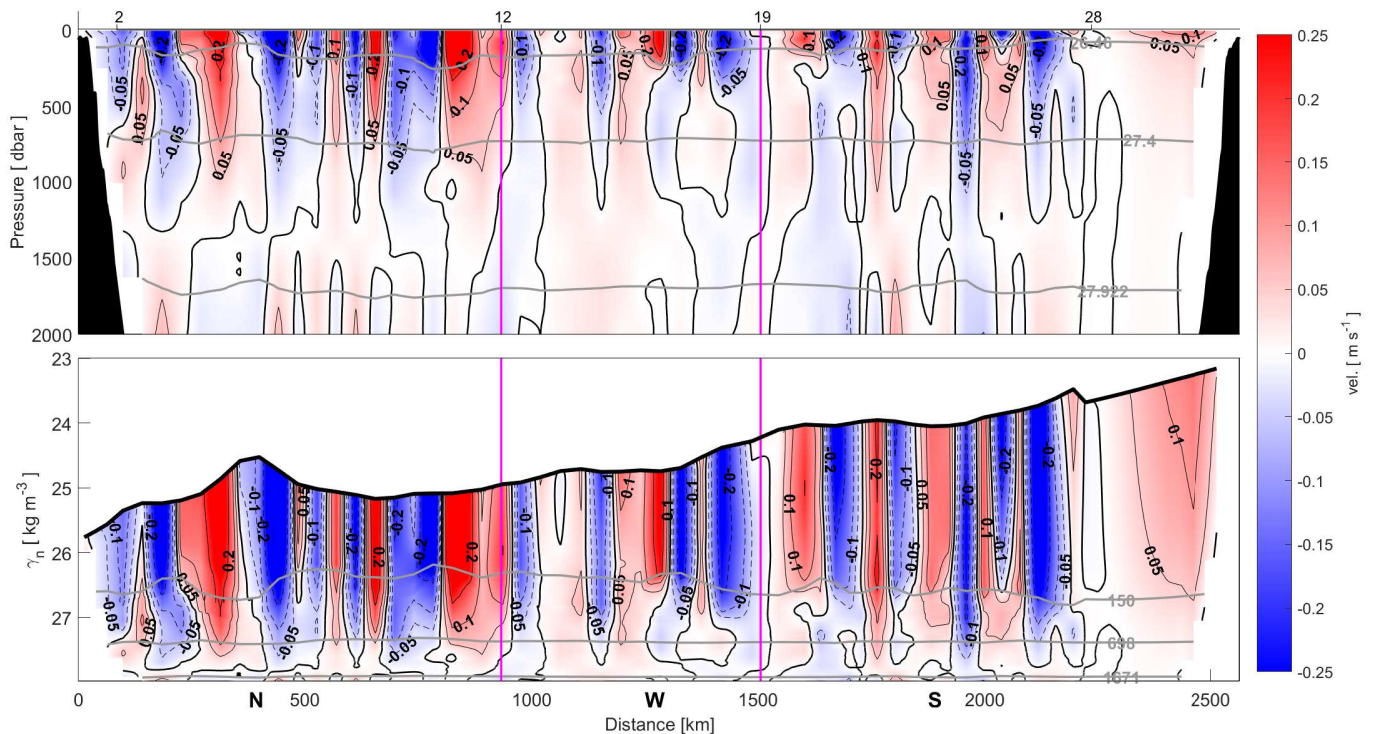
Figure A13. Sections of the absolute geostrophic velocity perpendicular to each transect with respect to depth (upper panel) and γ_n (lower panel) during FLUXES-I cruise (including WOA stations). The velocity sign was selected on geographic criteria (positive sign northward and eastward). The direction chosen for the representation is the same as in Fig. A3. Zero contour line is the thick black line. The N/W and W/S corners are indicated with vertical pink lines at stations 12 and 19. In depth sections, the isoneutrals which delimit the surface, central, intermediate and deep water are represented by grey contours. In γ_n sections, the depths of 150, 698 and 1671 m are also shown.
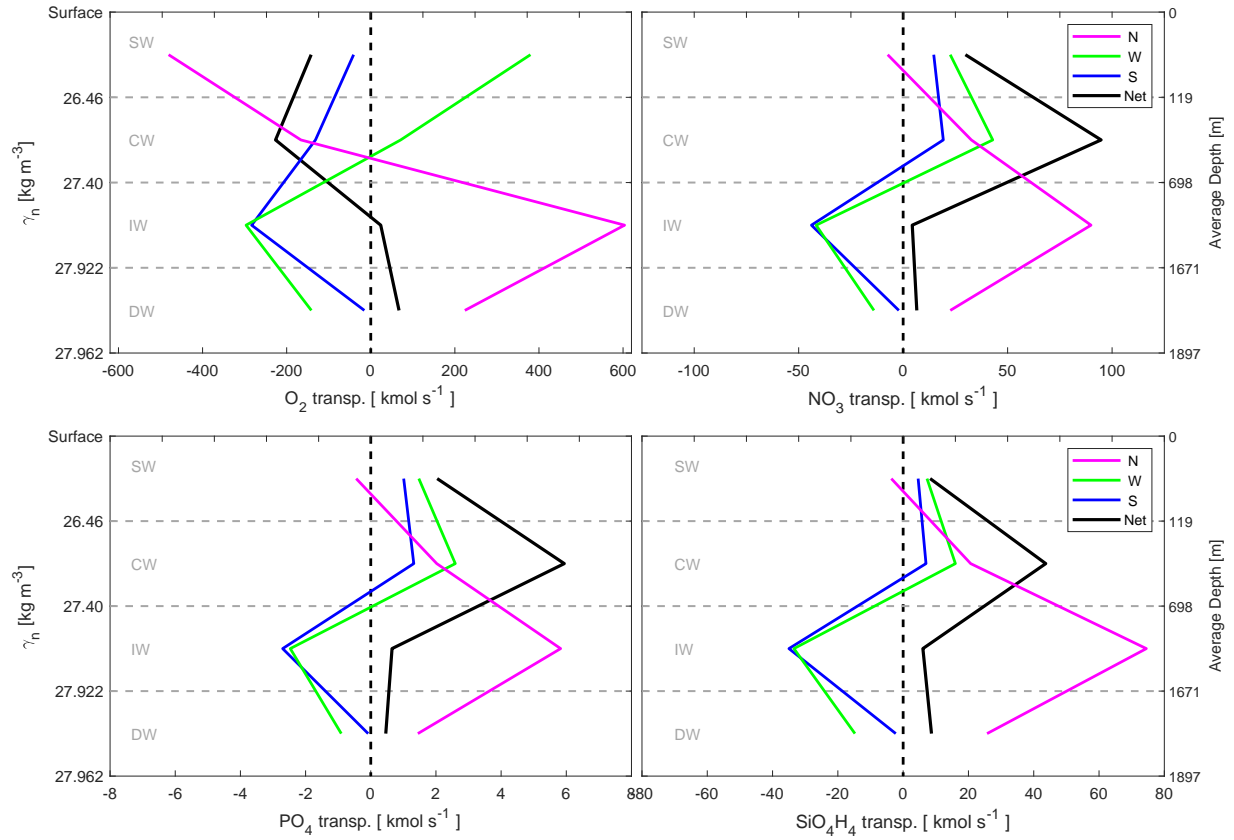
Figure A14. Mass (), O_2, NO_3, PO_4 and SiO_4H_4 transports ($\mathrm{kmol\,s^{-1}}$) integrated per water types levels (SW, CW, IW and DW) at transects north (N, pink line), west (W, green line) and south (S, blue line) during FLUXES-I cruise and including WOA stations. Black line represents the net transport of each biochemical variable. See Tab. A2 to check O_2, NO_3, PO_4 and SiO_4H_4 transports values at each layer per transect. Negative/positive values indicate inward/outward transports as in Fig. A11.
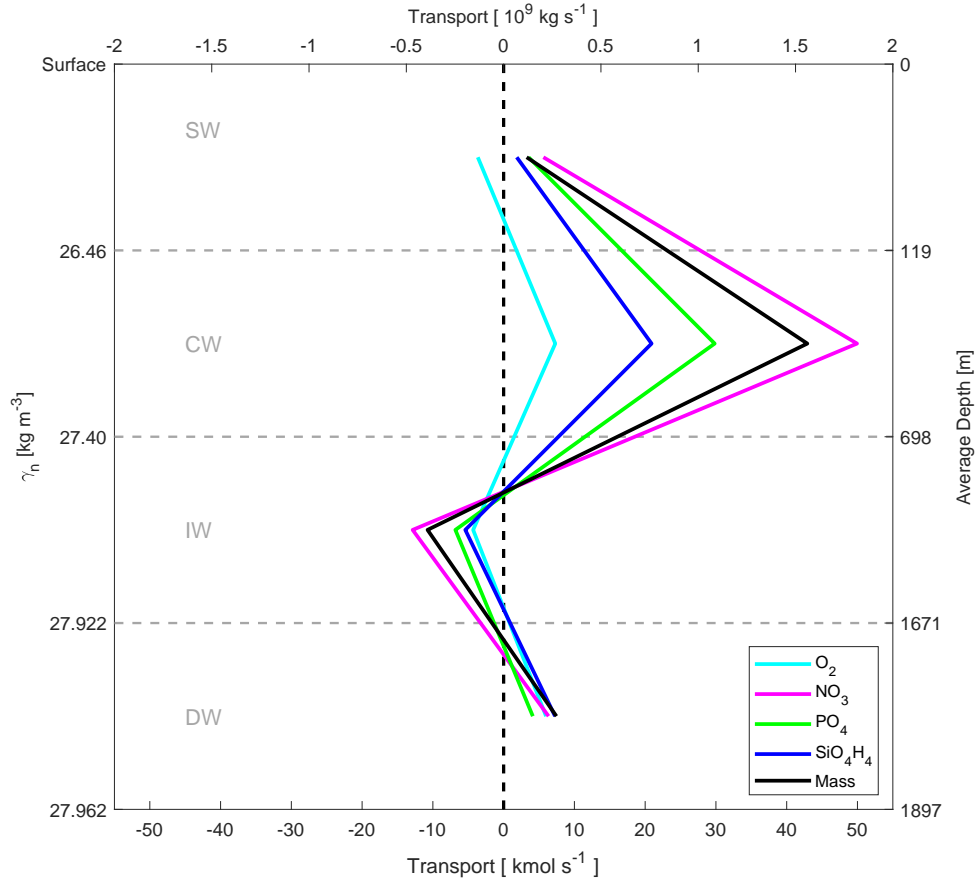
Figure A15. Mass ($10^9 \, \mathrm{kg \, s^{-1}}$), O_2, NO_3, PO_4 and SiO_4H_4 transports ($\mathrm{kmol \, s^{-1}}$) integrated per water types levels (SW, CW, IW and DW) through transect E during FLUXES-I cruise. Eastward transports were defined positive. The O_2/PO_4 transport is represented divided/multiplied by 10.
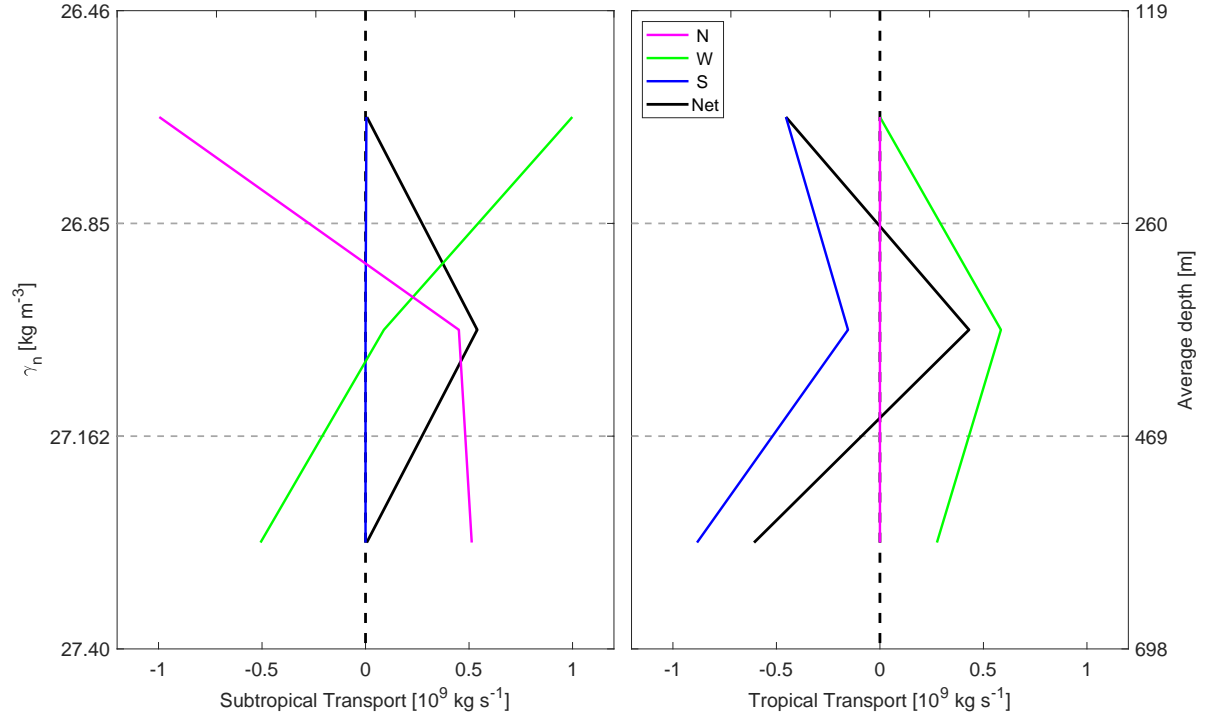
Figure A16. Mass transports ($10^9 \, \mathrm{kg \, s^{-1}}$) integrated per transect at north (N, pink line), west (W, green line) and south (S, blue line) of the subtropical (left) and tropical (right) areas separated by the CVF at the three CW layers and considering transports between WOA stations. Black line represents the net transport. Negative/positive values indicate inward/outward transports as in Fig. A11.

Table A1. A priori noise of equations corresponding to the SW, CW, IW and DW levels and uncertainties of all unknowns of inverse model.

WATER LEVELS	R_{nn} [Sv^2]
SW and CW	$[2.13 - 3.34]^2$
IW	$[2.88 - 3.49]^2$
DW	$[1.70]^2$
UNKNOWNS	R_{xx}
Velocities	$[10^{-4} - 10^{-3}]^2$ [ms^{-1}]^2
Ekman transports	$[10^{-5} - 10^{-4}]^2$ [Sv^2]
Freshwater flux	0.004^2 [Sv^2]

Table A2. Mass transports and their errors in Sv and transports of O_2, NO_3, PO_4 and SiO_4H_4 in $kmol\,s^{-1}$ with their errors relative to mass transport for SW, CW, IW, and DW across northern, western, southern and eastern transects for FLUXES-I cruise (with WOA stations). Positive/negative values indicate outward/inward transports. Total row of each inorganic nutrient or O_2 is its integrated transport in all the water column. The last column is the disajust or imbalance of each water level.

TRANSPORT	WATER LEVEL	NORTH	WEST	SOUTH	IMBALANCE
CW [Sv]	SW	-1.80 ± 0.75	2.32 ± 0.79	-0.89 ± 0.59	-0.37 ± 1.24
	CW	-0.03 ± 1.49	1.44 ± 1.62	-1.49 ± 1.73	-0.08 ± 2.80
	IW	3.43 ± 2.54	-1.52 ± 2.73	-1.87 ± 2.55	0.05 ± 4.52
	DW	0.99 ± 0.99	-0.62 ± 1.07	-0.06 ± 1.04	0.31 ± 1.79
	TOTAL	2.59 ± 3.19	1.62 ± 3.44	-4.31 ± 3.31	-0.09 ± 5.74
O_2 [$kmol\,s^{-1}$]	SW	-480.79 ± 198.59	379.80 ± 129.89	-40.79 ± 27.09	-141.77 ± 225.46
	CW	-166.13 ± 764.92	71.14 ± 79.95	-131.51 ± 152.72	-226.49 ± 489.00
	IW	603.63 ± 446.28	-296.60 ± 530.85	-283.33 ± 387.17	23.70 ± 794.27
	DW	223.75 ± 222.64	-141.27 ± 244.20	-15.25 ± 263.23	67.23 ± 222.93
	TOTAL	180.46 ± 222.42	13.08 ± 27.77	-470.88 ± 361.33	-277.34 ± 975.37
NO_3 [$kmol\,s^{-1}$]	SW	-7.39 ± 3.05	22.54 ± 7.71	14.65 ± 9.73	29.80 ± 47.39
	CW	32.64 ± 150.30	42.88 ± 48.19	19.22 ± 22.32	94.74 ± 204.5
	IW	89.91 ± 66.47	-41.65 ± 74.55	-43.90 ± 60.00	4.36 ± 242.61
	DW	22.56 ± 22.45	-13.97 ± 24.15	-2.06 ± 35.47	6.53 ± 21.70
	TOTAL	137.72 ± 169.74	9.80 ± 20.81	-12.09 ± 9.28	135.43 ± 476.30
PO_4 [$kmol\,s^{-1}$]	SW	-0.45 ± 0.18	1.47 ± 0.50	1.01 ± 0.67	2.04 ± 3.24
	CW	2.02 ± 9.32	2.59 ± 2.91	1.32 ± 1.53	5.94 ± 12.82
	IW	5.83 ± 4.31	-2.47 ± 4.42	-2.70 ± 3.69	0.65 ± 36.36
	DW	1.45 ± 1.44	-0.91 ± 1.56	-0.08 ± 1.37	0.46 ± 1.53
	TOTAL	8.85 ± 10.91	0.69 ± 1.47	-0.45 ± 0.35	9.09 ± 31.96
SiO_4H_4 [$kmol\,s^{-1}$]	SW	-3.63 ± 1.50	7.30 ± 2.50	4.59 ± 3.05	8.27 ± 13.15
	CW	20.68 ± 95.22	16.00 ± 17.98	7.00 ± 8.13	43.68 ± 94.29
	IW	74.49 ± 55.07	-33.46 ± 59.88	-34.98 ± 47.80	6.05 ± 336.72
	DW	25.70 ± 25.57	-14.76 ± 25.52	-2.26 ± 38.92	8.68 ± 28.71
	TOTAL	117.24 ± 144.50	-24.92 ± 52.92	-25.65 ± 19.68	66.67 ± 234.49

Table A3. Total imbalances of mass, O_2, NO_3, PO_4 and SiO_4H_4 transports in the subtropical and tropical areas separated by the CVF at the three CW layers. Imbalances on one side and on the other of the CVF are estimated from the integrated transports in one and other side of the front and considering transports between WOA stations.

TRANSPORT	SUBTROPICAL IMBALANCE	TROPICAL IMBALANCE
CW [Sv]	0.56 ± 1.47	-0.63 ± 1.68
O_2 [kmol s^{-1}]	-153.12 ± 714.98	-73.38 ± 134.08
NO_3 [kmol s^{-1}]	46.68 ± 133.26	47.07 ± 99.62
PO_4 [kmol s^{-1}]	2.88 ± 11.36	3.05 ± 6.20
SiO_4H_4 [kmol s^{-1}]	23.37 ± 109.32	20.32 ± 44.14

References

Álvarez, M. and Álvarez-Salgado, X. A.: Chemical tracer transport in the eastern boundary current system of the North Atlantic, Ciencias Marinas, 35, 123–139, 2009.

Anderson, L. A. and Sarmiento, J. L.: Redfield ratios of remineralization determined by nutrient data analysis, Global biogeochemical cycles, 8, 65–80, 1994.

Appen, W.-J. v., Strass, V. H., Bracher, A., Xi, H., Hörstmann, C., Iversen, M. H., and Waite, A. M.: High-resolution physical–biogeochemical structure of a filament and an eddy of upwelled water off northwest Africa, Ocean Science, 16, 253–270, 2020.

Barceló-Llull, B., Sangrà, P., Pallàs-Sanz, E., Barton, E. D., Estrada-Allis, S. N., Martínez-Marrero, A., Aguiar-González, B., Grisolía, D., Gordo, C., Rodríguez-Santana, Á., et al.: Anatomy of a subtropical intrathermocline eddy, Deep Sea Research Part I: Oceanographic Research Papers, 124, 126–139, 2017.

Barton, E.: Meanders, eddies and intrusions in the thermohaline front off Northwest Africa, Oceanologica acta, 10, 267–283, 1987.

Barton, E.: The poleward undercurrent on the eastern boundary of the subtropical North Atlantic, Springer, 1989.

Benazzouz, A., Mordane, S., Orbi, A., Chagdali, M., Hilmi, K., Atillah, A., Pelegrí, J. L., and Hervé, D.: An improved coastal upwelling index from sea surface temperature using satellite-based approach–The case of the Canary Current upwelling system, Continental Shelf Research, 81, 38–54, 2014a.

Benazzouz, A., Pelegrí, J. L., Demarcq, H., Machín, F., Mason, E., Orbi, A., Peña-Izquierdo, J., and Soumia, M.: On the temporal memory of coastal upwelling off NW Africa, Journal of Geophysical Research C: Oceans, 119, 6356–6380, https://doi.org/10.1002/2013JC009559, 2014b.

Bentamy, A. and Fillon, D. C.: Gridded surface wind fields from Metop/ASCAT measurements, International journal of remote sensing, 33, 1729–1754, 2012.

Brandt, P., Bange, H. W., Banyte, D., Dengler, M., Didwischus, S.-H., Fischer, T., Greatbatch, R. J., Hahn, J., Kanzow, T., Karstensen, J., et al.: On the role of circulation and mixing in the ventilation of oxygen minimum zones with a focus on the eastern tropical North Atlantic, Biogeosciences, 12, 489–512, 2015.

Broecker, W.: 'NO' A conservative-mass tracer, Earth Planet, Sci. Letters, 23, 100–107, 1974.

Burgoa, N., Machín, F., Marrero-Díaz, A., Rodríguez-Santana, A., Martínez-Marrero, A., Arístegui, J., and Duarte, C. M.: Mass, nutrients and dissolved organic carbon (DOC) lateral transports off northwest Africa during fall 2002 and spring 2003, Ocean Science, 16, 483–511, https://doi.org/10.5194/os-16-483-2020, https://os.copernicus.org/articles/16/483/2020/, 2020.

Capet, X., McWilliams, J. C., Molemaker, M. J., and Shchepetkin, A.: Mesoscale to submesoscale transition in the California Current System. Part II: Frontal processes, Journal of Physical Oceanography, 38, 44–64, 2008.

Castellanos, P., Pelegrí, J. L., Campos, E. J., Rosell-Fieschi, M., and Gasser, M.: Response of the surface tropical Atlantic Ocean to wind forcing, Progress in Oceanography, 134, 271–292, 2015.

Ekman, V. W.: Über Horizontalzirkulation bei winderzeugten Meeresströmungen, R. Friedländer & Sohn, 1923.

Emery, W. J.: Water types and water masses, Encyclopedia of ocean sciences, 6, 3179–3187, 2001.

Fernández-Castro, B., Mouriño-Carballido, B., and Álvarez-Salgado, X. A.: Non-redfieldian mesopelagic nutrient remineralization in the eastern North Atlantic subtropical gyre, Progress in Oceanography, 171, 136–153, 2019.

Fu, Y., Karstensen, J., and Brandt, P.: Atlantic Meridional Overturning Circulation at 14.5° N in 1989 and 2013 and 24.5° N in 1992 and 2015: volume, heat, and freshwater transports, Ocean Science, 14, 589–616, https://doi.org/10.5194/os-14-589-2018, https://www.ocean-sci.net/14/589/2018/, 2018.

Gabric, A. J., Garcia, L., Van Camp, L., Nykjaer, L., Eifler, W., and Schrimpf, W.: Offshore export of shelf production in the Cape Blanc (Mauritania) giant filament as derived from coastal zone color scanner imagery, Journal of Geophysical Research: Oceans, 98, 4697–4712, 1993.

Ganachaud, A.: Large-scale mass transports, water mass formation, and diffusivities estimated from World Ocean Circulation Experiment (WOCE) hydrographic data, Journal of Geophysical Research, 108, 3213, https://doi.org/10.1029/2002JC001565, http://doi.wiley.com/10.1029/2002JC001565, 2003a.

Ganachaud, A.: Error budget of inverse box models: The North Atlantic, Journal of Atmospheric and Oceanic Technology, 20, 1641–1655, 2003b.

Ganachaud, A. S.: Large Scale Oceanic Circulation and Fluxes of Freshwater, Heat, Nutrients and Oxygen, Ph.D. thesis, Massachusetts Institute of Technology and Woods Hole Oceanographic Institution, https://doi.org/10.1575/1912/4130, 1999.

Garcia, H. E., Locarnini, R. A., Boyer, T. P., Antonov, J. I., Baranova, O. K., Zweng, M. M., Reagan, J. R., and Johnson, D. R.: World Ocean Atlas 2013, Volume 3: Dissolved Oxygen, Apparent Oxygen Utilization, and Oxygen Saturation, NOAA Atlas NESDIS 75, p. 27, 2014a.

Garcia, H. E., Locarnini, R. A., Boyer, T. P., Antonov, J. I., Baranova, O. K., Zweng, M. M., Reagan, J. R., and Johnson, D. R.: World Ocean Atlas 2013, Volume 4: Dissolved Inorganic Nutrients (phosphate, nitrate, silicate), NOAA Atlas NESDIS 76, p. 25, 2014b.

Grasshoff, K., Ehrhardt, M., and Kremling, K.: Determination of nutrients, Methods of Seawater Analysis, p. 159–228, 1999.

Hempel, G.: The Canary Current:Studies of an Upwelling System, A Symposium held in Las Palmas, 11-14 April 1978, Secretariat of the International Council for the Exploration of the Sea, 180, 1982.

Hernández-Guerra, A., Fraile-Nuez, E., López-Laatzen, F., Martínez, A., Parrilla, G., and Vélez-Belchí, P.: Canary Current and North Equatorial Current from an inverse box model, Journal of Geophysical Research: Oceans, 110, 1–16, https://doi.org/10.1029/2005JC003032, 2005.

Hernández-Guerra, A., Espino-Falcón, E., Vélez-Belchí, P., Pérez-Hernández, M. D., Martínez-Marrero, A., and Cana, L.: Recirculation of the Canary Current in fall 2014, Journal of Marine Systems, 174, 25–39, https://doi.org/10.1016/j.jmarsys.2017.04.002, 2017.

Hosegood, P., Nightingale, P., Rees, A., Widdicombe, C., Woodward, E., Clark, D., and Torres, R.: Nutrient pumping by submesoscale circulations in the mauritanian upwelling system, Progress in Oceanography, 159, 223–236, 2017.

Hughes, P. and Barton, E. D.: Stratification and water mass structure in the upwelling area off northwest Africa in April/May 1969, Deep-Sea Research and Oceanographic Abstracts, 21, https://doi.org/10.1016/0011-7471(74)90046-1, 1974.

IOC, SCOR, and IAPSO: IAPSO, 2010: The International Thermodynamic Equation of Seawater—2010: Calculation and use of thermodynamic properties, Intergovernmental Oceanographic Commission, Manuals and Guides, 56, 220, 2010.

Jackett, D. R. and McDougall, T. J.: A Neutral Density Variable for the World's Oceans, Journal of Physical Oceanography, 27, 237–263, 1997.

Karstensen, J. and Tomczak, M.: Age determination of mixed water masses using CFC and oxygen data, Journal of Geophysical Research: Oceans, 103, 18 599–18 609, 1998.

Karstensen, J., Stramma, L., and Visbeck, M.: Oxygen minimum zones in the eastern tropical Atlantic and Pacific oceans, Progress in Oceanography, 77, 331–350, 2008.

Kawase, M. and Sarmiento, J. L.: Nutrients in the Atlantic thermocline, Journal of Geophysical Research: Oceans, 90, 8961–8979, 1985.

Lázaro, C., Fernandes, M. J., Santos, A. M. P., and Oliveira, P.: Seasonal and interannual variability of surface circulation in the Cape Verde region from 8 years of merged T/P and ERS-2 altimeter data, Remote Sensing of Environment, 98, 45–62, https://doi.org/10.1016/j.rse.2005.06.005, 2005.

Locarnini, R. A., Mishonov, A. V., Antonov, J. I., Boyer, T. P., Garcia, H. E., Baranova, O. K., Zweng, M. M., Paver, C. R., Reagan, J. R.,
5   Johnson, D. R., Hamilton, M., and Seidov, D.: World Ocean Atlas 2013, Volume 1: Temperature, NOAA Atlas NESDIS 73, p. 44, 2013.

Locarnini, R. A., Mishonov, A. V., Baranova, O. K., Boyer, T. P., Zweng, M. M., Garcia, H. E., Reagan, J. R., Seidov, D., Weathers, K., Paver, C. R., and Smolyar, I.: World Ocean Atlas 2018, Volume 1: Temperature, NOAA Atlas NESDIS 81, p. 52, 2018.

Lønborg, C. and Álvarez-Salgado, X. A.: Tracing dissolved organic matter cycling in the eastern boundary of the temperate North Atlantic using absorption and fluorescence spectroscopy, Deep Sea Research Part I: Oceanographic Research Papers, 85, 35–46, 2014.

10   Lovecchio, E., Gruber, N., and Münnich, M.: Mesoscale contribution to the long-range offshore transport of organic carbon from the Canary Upwelling System to the open North Atlantic, Biogeosciences, 15, 5061–5091, 2018.

Luyten, J., Pedlosky, J., and Stommel, H.: The ventilated thermocline, Journal of Physical Oceanography, 13, 292–309, 1983.

Machín, F.: Variabilidad espacio temporal de la Corriente de Canarias, del afloramiento costero al noroeste de África y de los intercambios atmósfera-océano de calor y agua dulce, Ph.D. thesis, Universidad de Las Palmas de Gran Canaria, 2003.

15   Machín, F. and Pelegrí, J. L.: Northward penetration of Antarctic intermediate water off Northwest Africa, Journal of Physical Oceanography, 39, 512–535, 2009.

Machín, F., Hernández-Guerra, A., and Pelegrí, J. L.: Mass fluxes in the Canary Basin, Progress in Oceanography, 70, 416–447, https://doi.org/10.1016/j.pocean.2006.03.019, 2006.

Machín, F., Pelegrí, J. L., Fraile-Nuez, E., Vélez-Belchí, P., López-Laatzen, F., and Hernández-Guerra, A.: Seasonal Flow Reversals of
20   Intermediate Waters in the Canary Current System East of the Canary Islands, Journal of Physical Oceanography, 40, 1902–1909, https://doi.org/10.1175/2010JPO4320.1, http://journals.ametsoc.org/doi/abs/10.1175/2010JPO4320.1, 2010.

Martel, F. and Wunsch, C.: The North Atlantic Circulation in the Early 1980s-An Estimate from Inversion of a Finite-Difference Model, Journal of Physical Oceanography, 23, 898–924, 1993.

Martínez-Marrero, A., Rodríguez-Santana, A., Hernández-Guerra, A., Fraile-Nuez, E., López-Laatzen, F., Vélez-Belchí, P., and Parrilla,
25   G.: Distribution of water masses and diapycnal mixing in the Cape Verde Frontal Zone, Geophysical Research Letters, 35, 0–4, https://doi.org/10.1029/2008GL033229, 2008.

MATLAB: version R2019b, The MathWorks Inc., Natick, Massachusetts, https://www.mathworks.com/products/matlab.html, 2019.

McDougall, T., Jackett, D., Millero, F. J., Pawlowicz, R., and Barker, P.: A global algorithm for estimating Absolute Salinity., Ocean Science, 8, 2012.

30   McDougall, T. J. and Barker, P. M.: Getting started with TEOS-10 and the Gibbs Seawater (GSW) oceanographic toolbox, SCOR/IAPSO WG, 127, 1–28, 2011.

Meunier, T., Barton, E. D., Barreiro, B., and Torres, R.: Upwelling filaments off Cap Blanc: Interaction of the NW African upwelling current and the Cape Verde frontal zone eddy field?, Journal of Geophysical Research: Oceans, 117, 2012.

Paillet, J. and Mercier, H.: An inverse model of the eastern North Atlantic general circulation and thermocline ventilation, Deep-Sea Research
35   Part I: Oceanographic Research Papers, 44, 1293–1328, https://doi.org/10.1016/S0967-0637(97)00019-8, 1997.

Pastor, M. V., Pelegrí, J. L., Hernández-Guerra, A., Font, J., Salat, J., and Emelianov, M.: Water and nutrient fluxes off Northwest Africa, Continental Shelf Research, 28, 915–936, 2008.

Pastor, M. V., Peña-Izquierdo, J., Pelegrí, J. L., and Marrero-Díaz, Á.: Meridional changes in water mass distributions off NW Africa during November 2007/2008, Ciencias Marinas, 38, 223–244, 2012.

Pastor, M. V., Palter, J. B., Pelegrí, J. L., and Dunne, J. P.: Physical drivers of interannual chlorophyll variability in the eastern subtropical North Atlantic, Journal of Geophysical Research: Oceans, 118, 3871–3886, https://doi.org/10.1002/jgrc.20254, 2013.

5 Pelegrí, J. L. and Benazzouz, A.: Oceanographic and biological features in the Canary Current Large Marine Ecosystem, Chapter 3.4, Coastal Upwelling off north-west Africa, IOC Technical Series, 115, 2015a.

Pelegrí, J. L. and Benazzouz, A.: Oceanographic and biological features in the Canary Current Large Marine Ecosystem, Chapter 4.1, Inorganic nutrients and dissolved oxygen in the Canary Current large marine ecosystem, IOC Technical Series, 115, 2015b.

Pelegrí, J. L., Arístegui, J., Cana, L., González-Dávila, M., Hernández-Guerra, A., Hernández-León, S., Marrero-Díaz, A., Montero, M. F.,
10 Sangrà, P., and Santana-Casiano, M.: Coupling between the open ocean and the coastal upwelling region off northwest Africa: Water recirculation and offshore pumping of organic matter, Journal of Marine Systems, 54, 3–37, https://doi.org/10.1016/j.jmarsys.2004.07.003, 2005.

Pelegrí, J. L., Marrero-Díaz, A., and Ratsimandresy, A. W.: Nutrient irrigation of the North Atlantic, Progress in Oceanography, 70, 366–406, https://doi.org/10.1016/j.pocean.2006.03.018, 2006.

15 Pelegrí, J. L., Peña-Izquierdo, J., Machín, F., Meiners, C., and Presas-Navarro, C.: Deep-Sea Ecosystems Off Mauritania, Chapter 3, Oceanography of the Cape Verde Basin and Mauritanian Slope Waters, Springer, https://doi.org/10.1007/978-94-024-1023-5_3, http://api.elsevier.com/content/abstract/scopus_id/85035361292, 2017.

Peña-Izquierdo, J., Pelegrí, J. L., Pastor, M. V., Castellanos, P., Emelianov, M., Gasser, M., Salvador, J., and Vázquez-Domínguez, E.: The continental slope current system between Cape Verde and the Canary Islands, Scientia Marina, 76, 65–78,
20 https://doi.org/10.3989/scimar.03607.18C, 2012.

Peña-Izquierdo, J., van Sebille, E., Pelegrí, J. L., Sprintall, J., Mason, E., Llanillo, P. J., and Machín, F.: Water mass pathways to the North Atlantic oxygen minimum zone, Journal of Geophysical Research: Oceans, 120, 3350–3372, 2015.

Pérez, F. F., Mintrop, L., Llinás, O., Glez-Dávila, M., Castro, C. G., Alvarez, M., Körtzinger, A., Santana-Casiano, M., Rueda, M. J., and Ríos, A. F.: Mixing analysis of nutrients, oxygen and inorganic carbon in the Canary Islands region, Journal of Marine Systems, 28,
25 183–201, https://doi.org/10.1016/S0924-7963(01)00003-3, 2001.

Pérez-Hernández, M. D., Hernández-Guerra, A., Fraile-Nuez, E., Comas-Rodríguez, I., Benítez-Barrios, V. M., Domínguez-Yanes, J. F., Vélez-Belchí, P., and De Armas, D.: The source of the Canary current in fall 2009, Journal of Geophysical Research: Oceans, 118, 2874–2891, https://doi.org/10.1002/jgrc.20227, 2013.

Pérez-Rodríguez, P., Pelegrí, J. L., and Marrero-Díaz, A.: Dynamical characteristics of the Cape Verde frontal zone, Scientia Marina, 65,
30 241–250, https://doi.org/10.3989/scimar.2001.65s1241, 2001.

Powers, J. G., Klemp, J. B., Skamarock, W. C., Davis, C. A., Dudhia, J., Gill, D. O., Coen, J. L., Gochis, D. J., Ahmadov, R., Peckham, S. E., et al.: The weather research and forecasting model: Overview, system efforts, and future directions, Bulletin of the American Meteorological Society, 98, 1717–1737, 2017.

Sangrà, P., Pascual, A., Rodríguez-Santana, Á., Machín, F., Mason, E., McWilliams, J. C., Pelegrí, J. L., Dong, C., Rubio, A., Arístegui,
35 J., Marrero-Díaz, Á., Hernández-Guerra, A., Martínez-Marrero, A., and Auladell, M.: The Canary Eddy Corridor: A major pathway for long-lived eddies in the subtropical North Atlantic, Deep-Sea Research Part I: Oceanographic Research Papers, 56, 2100–2114, https://doi.org/10.1016/j.dsr.2009.08.008, 2009.

Siedler, G., Zangenberg, N., Onken, R., and Morlière, A.: Seasonal changes in the tropical Atlantic circulation: Observation and simulation of the Guinea Dome, Journal of Geophysical Research: Oceans, 97, 703–715, 1992.

Smith, W. H. F. and Sandwell, D. T.: Global Sea Floor Topography from Satellite Altimetry and Ship Depth Soundings, Science, 277, 1956–1962, https://doi.org/10.1126/science.277.5334.1956, http://science.sciencemag.org/content/277/5334/1956, 1997.

Stramma, L.: Geostrophic transport in the warm water sphere of the eastern subtropical North Atlantic, Journal of Marine Research, 42, 537–558, https://doi.org/10.1357/002224084788506022, 1984.

Stramma, L. and Siedler, G.: Seasonal changes in the North Atlantic subtropical gyre, Journal of Geophysical Research: Oceans, 93, 8111–8118, 1988.

Thomas, L. N.: Formation of intrathermocline eddies at ocean fronts by wind-driven destruction of potential vorticity, Dynamics of Atmospheres and Oceans, 45, 252–273, 2008.

Thomsen, S., Karstensen, J., Kiko, R., Krahmann, G., Dengler, M., and Engel, A.: Remote and local drivers of oxygen and nitrate variability in the shallow oxygen minimum zone off Mauritania in June 2014, Biogeosciences, 16, 979–998, 2019.

Tomczak, M.: The CINECA experience, Marine Policy, 3, 59–65, https://doi.org/https://doi.org/10.1016/0308-597X(79)90040-X, 1979.

Tomczak, Jr, M.: An analysis of mixing in the frontal zone of South and North Atlantic Central Water off North-West Africa, Progress in Oceanography, 10, 173–192, https://doi.org/10.1016/0079-6611(81)90011-2, 1981.

Troupin, C., Barth, A., Sirjacobs, D., Ouberdous, M., Brankart, J.-M., Brasseur, P., Rixen, M., Alvera-Azcárate, A., Belounis, M., Capet, A., et al.: Generation of analysis and consistent error fields using the Data Interpolating Variational Analysis (DIVA), Ocean Modelling, 52, 90–101, 2012.

UNESCO: The international system of units (SI) in oceanography, Technical Paper in Marine Science, 45, 1–124, 1985.

Volkov, D. L., Lee, T., and Fu, L.-L.: Eddy-induced meridional heat transport in the ocean, Geophysical Research Letters, 35, 2008.

Wanninkhof, R.: Relationship between wind speed and gas exchange over the ocean revisited, Limnology and Oceanography: Methods, 12, 351–362, 2014.

Wunsch, C.: North Atlantic general circulation west of $50°$W determined by inverse methods, Reviews of Geophysics, 16, 583–620, 1978.

Zenk, W., Klein, B., and Schroder, M.: Cape Verde Frontal Zone, Deep Sea Research Part A. Oceanographic Research Papers, 38, S505–S530, https://doi.org/10.1016/S0198-0149(12)80022-7, 1991.

Zhang, Z., Wang, W., and Qiu, B.: Oceanic mass transport by mesoscale eddies, Science, 345, 322–324, 2014.

Zweng, M. M., Reagan, J. R., Antonov, J. I., Locarnini, R. A., Mishonov, A. V., Boyer, T. P., Garcia, H. E., Baranova, O. K., Johnson, D. R., Seidov, D., and Biddle, M. M.: World Ocean Atlas 2013, Volume 2: Salinity, NOAA Atlas NESDIS 74, p. 39, 2013.

Zweng, M. M., Reagan, J. R., Seidov, D., Boyer, T. P., Locarnini, R. A., Garcia, H. E., Mishonov, A. V., Baranova, O. K., Weathers, K., Paver, C. R., and Smolyar, I.: World Ocean Atlas 2018, Volume 2: Salinity, NOAA Atlas NESDIS 82, p. 50, 2018.